Check for updates

Accepted Article

Linking Deep and Shallow Convective Mass Fluxes via an Assumed Entrainment Distribution in CAM5-CLUBB: Parameterization and Simulated Precipitation Variability

Ben Yang[1,2], Minghuai Wang[1,3], Guang J. Zhang[4], Zhun Guo[5], Anning Huang[1,2], and Yaocun Zhang[1,2], Yun Qian[6]

[1] School of Atmospheric Sciences, Nanjing University, Nanjing, China

[2] CMA-NJU Joint Laboratory for Climate Prediction Studies, Nanjing University, Nanjing, China

[3] Joint International Research Laboratory of Atmospheric and Earth System Sciences & Institute for Climate and Global Change Research, Nanjing University, Nanjing, China

[4] Scripps Institution of Oceanography, University of California, San Diego, La Jolla, California, USA

[5] State Key Laboratory of Numerical Modeling for Atmospheric Sciences and Geophysical Fluid Dynamics, Institute of Atmospheric Physics, Chinese Academy of Sciences, Beijing, China

[6] Pacific Northwest National Laboratory, Richland, Washington, USA

Correspondence to Ben Yang byang@nju.edu.cn

Revised to *Journal of Advances in Modeling Earth Systems*

January 2021

This article has been accepted for publication and undergone full peer review but has not been through the copyediting, typesetting, pagination and proofreading process, which may lead to differences between this version and the Version of Record. Please cite this article as doi: 10.1029/2020MS002357.

This article is protected by copyright. All rights reserved.

Accepted Article

Abstract

We modify the Zhang-McFarlane deep convection scheme in the Community Atmosphere Model version 5 to couple it with a unified parameterization for boundary-layer turbulence and shallow convection, i.e. Cloud Layers Unified by Binormals (CLUBB). By assuming a lognormal distribution of entrainment rate across the entire moist convective regimes, we link mass fluxes between shallow and deep convection, which are partitioned by the entrainment rate of the shallowest deep convective plume. Hence, a new deep convective closure is established which is coupled to the sub-grid vertical motion variability in CLUBB. The convection feedback (or memory) effects are also considered to decrease the entrainment spectrum width and enhance the vertical velocity variability that further affect deep convection. Results show that the revised scheme improves the precipitation simulations in terms of the mean state and variability at various timescales, such as the alleviated double-intertropical convergence zone and more realistic simulations of the seasonal variation of monsoon precipitation over East Asia, Madden□Julian Oscillation, and precipitation diurnal phase propagations downstream of large terrains. The improvements are still seen in many aspects such as the mean-state precipitation when turning off the convection feedback impacts in the revised scheme, emphasizing the benefits of using the modified mass-flux closure. However, the convection feedbacks have considerable effects on the precipitation diurnal cycle simulations over regions with late-afternoon precipitation peaks. Overall, the revised scheme provides a unified treatment for sub-grid vertical motions across regimes of boundary-layer turbulence, shallow convection and deep convection, leading to better-simulated precipitation at various timescales.

This article is protected by copyright. All rights reserved.

Accepted Article

Keywords: Deep and Shallow Convection; Mass Flux; Entrainment Distribution; Precipitation Simulation; Zhang–McFarlane Parameterization; CLUBB

Plain Language Summary

The physical consistency between shallow and deep convection is an important but largely misrepresented aspect in climate models. In the atmosphere, convective updraft plumes usually differ in their fractional entrainment rate, with weaker entrainment favoring a more vertical extension of the plume. Here, we modify the Zhang-McFarlane convective parameterization in CAM5 to couple it with a unified parameterization for boundary-layer turbulence and shallow convection, i.e. CLUBB. A continuous distribution is used to represent the spectrum of entrainment rates across the entire moist convective regimes and to link mass fluxes between shallow and deep convection. This couples deep convection to CLUBB and provides a unified treatment for sub-grid vertical motions across regimes of boundary-layer turbulence, shallow convection and deep convection. In addition, the convection memory effects are included to affect deep convection via changing the entrainment spectrum width and vertical velocity variability. The revised scheme performs much better than the original one in the simulated precipitation variability at various timescales, such as the alleviated double-intertropical convergence zone and improved monsoon precipitation, Madden□Julian Oscillation, and continental precipitation diurnal variation. Both of the modifications related to the mass flux closure and convection feedback impacts are important for the improved model performance.

This article is protected by copyright. All rights reserved.

Accepted Article

1 Introduction

Cumulus convection mainly induced by surface fluxes, large-scale convergence, and atmospheric radiative cooling can occur at a wide range of temporal and spatial scales in the globe (Arakawa, 2004; Rio et al., 2019). It is of vital importance to cloud and precipitation formation and can interact with the latent heating associated with precipitation process. Moreover, cumulus convection is key for redistributing atmospheric heat and moisture and modulating the energy and hydrological cycles on the Earth (Arakawa & Schubert 1974; Raymond 1994). However, it is hard to represent convection in both global and regional climate models (GCMs and RCMs) that are generally unable to explicitly resolve the fine-scale convective processes. As a result, convective parameterizations have to be used in these models to formulate the statistical effects on the grid-mean atmospheric properties of convection (Arakawa, 2004).

Many convective parameterizations have been developed with different levels of complexity (Arakawa & Schubert, 1974; Kain & Fritsch, 1990; Zhang & McFarlane, 1995; Emanuel & Zivkovic-Rothman, 1999; Grell & Devenyi, 2002; Song & Zhang, 2011; Park et al., 2014a). These parameterizations have large uncertainties in their physical assumptions and tunable parameters. In GCMs, many cloud and precipitation biases in terms of both the mean state (e.g. the spurious double intertropical convergence zone [ITCZ], unrealistic partitioning between convective and stratiform precipitation, etc.) and variability at various scales (e.g. incorrect diurnal phase of continental precipitation, underestimated Madden□Julian Oscillation [MJO; Madden & Julian, 1971], etc.) are attributed, at least in part, to deficiencies in convective parameterizations (e.g., Yang et al., 2013; Yuan et al. 2013; Zhang et al., 2019; Xie et al., 2019). To avoid the large uncertainties and systematic biases associated with convective parameterizations, some climate models are now run at

This article is protected by copyright. All rights reserved.

Accepted Article

convection-permitting scales that can partly or even entirely resolve convective processes owing to the rapid growth of computing power (Dirmeyer et al., 2012; Li et al., 2018; Marsham et al., 2013; Sato et al., 2008; Stratton & Stirling, 2012; Tsushima et al., 2014). An alternate but much less expensive approach is to run super□parameterized models that use cloud□resolving model instead of convective parameterization in each grid cell of a GCM (Grabowski, 2001; Khairoutdinov et al., 2005; Kooperman et al., 2013; Randall et al., 2003; Zhang & Chen, 2016; Zhang et al., 2017; Hannah et al., 2020).

However, undoubtedly, parameterization itself is a summary of our knowledge about the real atmosphere and its performance can reflect how well we understand the physical processes it represents (Rio et al., 2019). Recently, Emanuel (2020) pointed out that we need to make efforts to find out the reason why climate models with convective parameterizations fail to produce the large-scale precipitation phenomenon if such phenomenon is "parameterizable" (i.e., not sensitive to the detailed arrangement of individual convective cells), suggesting that we might compute too much and think too little. In addition, due to the needs for long integration length and multiple ensemble members, climate simulations adopted in climate change projection still use relatively coarse grid spacing (Eyring et al., 2016). Therefore, it is still necessary to continue the development of convection parameterizations.

Many efforts have been devoted to improving the behaviors of convective parameterizations in the past decades. For example, Zhang and Wang (2006) applied a convective closure based on the large-scale generation of convective available potential energy (CAPE) in the free troposphere (Zhang, 2002) in the Zhang-McFarlane (ZM) convective parameterization in the National Center for Atmospheric Research (NCAR) Community Climate System Model version 3. Compared to the

This article is protected by copyright. All rights reserved.

Accepted Article

original version that used the total CAPE consumption as a closure, their new closure reduced the sensitivity of convection to surface forcing and thus alleviated the double-ITCZ problem. Meanwhile, several studies have shown that the simulated precipitation diurnal cycle can be improved via using different functions for convection triggering (Xie & Zhang, 2000; Tawfik et al., 2017; Xie et al., 2019), employing new diagnostic or prognostic quantities for convective closure (Fuchs & Raymond, 2007), or modifying the formulation of convective entrainment rates (Piriou et al., 2007; Stirling & Stratton, 2012). It was also reported that structural modifications or parameter optimizations in convective parameterizations can improve the simulations of MJO and ENSO (Boyle et al., 2015; Lu & Ren, 2016; Liu et al., 2019; Neale et al., 2008) in GCMs.

In convective parameterizations, one of the well-known deficiencies is the unrealistic transition from shallow to deep convection, which is thought to be responsible for many of the cloud and precipitation biases mentioned above. Various approaches have been proposed to overcome this problem. For example, Bechtold et al. (2014) modified the CAPE-based closure in which parts of the CAPE production are consumed by shallow convection under particular conditions. Alternately, Rio et al. (2009) linked the triggering and intensity of deep convection to boundary-layer thermals that can reach the lifting condensation level (LCL). Both the above two approaches help improve the precipitation diurnal cycle simulations over land. Park (2014a; 2014b) developed a new parameterization that represents shallow and deep convection in a unified way, which can better simulate the continental precipitation diurnal variation and the MJO. Several fully unified parameterizations were also presented in some studies that included boundary-layer turbulence and all types of convection in a single framework (Storer et al., 2015; Tan et al., 2018; Sušelj et al., 2019). For example, Sušelj et al. (2019) extended the eddy-diffusivity mass-flux (EDMF) approach

This article is protected by copyright. All rights reserved.

Accepted Article

to contain multiple plumes representing dry, shallow, and deep convective updrafts and precipitation-driven downdrafts. The new parameterization can well simulate the transitions across various convective regimes in a single-column model (SCM).

In our recent work (Yang et al., 2020), we modified the ZM deep convective closure in the Community Atmosphere Model version 5 (CAM5; Neale et al., 2010) coupled with a third□order turbulence closure parameterization, i.e. Cloud Layers Unified by Binormals (CLUBB; Golaz et al., 2002; Larson & Golaz, 2005) (hereafter CAM5-CLUBB). In the modified closure, a part of CAPE diagnosed from the heating and moistening profiles in CLUBB is reserved for shallow convection, which helps suppress deep convection until shallow convection has sufficiently moistened the lower troposphere, leading to improved precipitation diurnal cycle simulation. However, compared to the original closure, the modified one still shows similar bias features in many aspects, such as the spurious double-ITCZ, too weak MJO, and unrealistic monsoon migration. Besides, inconsistency still exists between different components within the ZM scheme. Specifically, the closure is based on CAPE which is calculated with a fixed entrainment rate for an air parcel lifted from the convective launch layer, while the updraft cloud properties are based on an ensemble of plumes with a range of different entrainment rates. To improve the consistency between shallow and deep convection, as well as between the deep convective closure and updraft plumes, here we modify the closure of the ZM convective parameterization and couple it with CLUBB to provide a unified treatment for sub-grid vertical motions across regimes of boundary-layer turbulence, shallow convection and deep convection. A lognormal distribution is assumed to represent the spectrum of entrainment rates across the entire moist convective regimes, with the spectrum width varying with the development of convection. The entrainment rate of the shallowest plume for deep

This article is protected by copyright. All rights reserved.

Accepted Article

convection is used to partition mass fluxes between deep and shallow convection, with the latter diagnosed from CLUBB. We will show that the revised ZM scheme markedly improves the simulated precipitation variability at various timescales in CAM5-CLUBB.

Section 2 depicts the modifications in the ZM convective parameterization scheme, including those related to the assumed distribution of entrainment rate, deep convective closure, and impacts of convection feedback. The model experiments and observational datasets are introduced in section 3. In section 4 we evaluate the impacts of the modified scheme on the precipitation simulation at various timescales. We first assess the results from the SCM experiments briefly and then focus on the GCM simulated precipitation in terms of the mean state, seasonal evolution, MJO, and diurnal variation. A summary of the main results is given in section 5.

2 Revised Zhang–McFarlane deep convective parameterization

2.1 Convective closure based on assumed entrainment distribution

In the original ZM scheme, the updraft cloud ensemble consists of multiple updraft plumes featured by different fractional entrainment rates (λ) to represent clouds reaching different heights. The shallowest deep convective plume has the maximum entrainment rate λ_0 and detrains at height z_0 corresponding to the minimum saturated moist static energy in the vertical. Therefore, the updraft plumes with entrainment rate exceeding λ_0 and detraining below z_0 can be categorized as shallow convection, which is not parameterized in ZM but implicitly represented by CLUBB that provides a unified treatment for boundary-layer turbulence and shallow convection. Previous studies have used the entrainment rates diagnosed from large-eddy simulations to evaluate the distributions of entrainment rate in convective parameterizations (e.g., de Rooy et al. 2013). Recently, based on

This article is protected by copyright. All rights reserved.

a large number of samples of aircraft measurements, Lu et al. (2012) and Guo et al. (2015) estimated the entrainment rates for shallow convective clouds over the US Southern Great Plains (SGP) and deep convective clouds over the western Pacific, respectively. Their results revealed that in both regimes the entrainment rate (λ; in units of km^{-1}) follows a lognormal distribution:

$$f(\lambda) = \frac{1}{\lambda\sigma\sqrt{2\pi}} e^{-\frac{1}{2}\left(\frac{\ln(\lambda/\eta)-\mu}{\sigma}\right)^2} , \quad (1)$$

but the values of μ and σ (i.e., the mean value and standard deviation of $\ln(\lambda)$, respectively) are different between the shallow and deep convective regimes. Here, we add a scaling factor η in Eq. 1 that is set to 1.0 by default, aiming to adjust the mean value of $\ln(\lambda)$ from μ to $\mu + \ln(\eta)$. Therefore, we can use one lognormal distribution to cover the entire moist convective regimes by allowing the width of the spectrum (i.e. η) to decrease with the development of convection (see section 2.2). In Eq. 1, μ and σ are set to 0.5 and 0.65, respectively. As η decreases, the distribution gradually evolves from the shallow convective regime as in Lu et al. (2012) toward the deep convective regime as in Guo et al. (2015).

The value of λ_0 corresponding to the shallowest deep convective plume is used to partition mass fluxes between deep and shallow convection (i.e., M_{deep} and M_{shallow}) (Fig. 1), and those with entrainment rates above and below λ_0 are categorized as shallow and deep convection, respectively. The partitioning is performed at the height of LCL (i.e., z_{LCL}) where the mass flux diagnosed in CLUBB has a close relationship with the strength of moist shallow convection. According to the entrainment distribution $f(\lambda)$ in Eq. 1, the relationship between M_{deep} and M_{shallow} at LCL is given by:

$$M_{\mathrm{deep}}(z_{\mathrm{LCL}}) = M_{\mathrm{shallow}}(z_{\mathrm{LCL}}) \frac{\int_{\lambda_{\min}}^{\lambda_0} f(\lambda)d\lambda}{\int_{\lambda_0}^{+\infty} f(\lambda)d\lambda} , \quad (2)$$

This article is protected by copyright. All rights reserved.

Accepted Article

Accepted Article

where $\lambda_{\min}$ is the minimum entrainment rate for deep convection. Because λ is inversely proportional to cloud radius as indicated by previous studies (e.g., Kain, 2004; de Rooy et al., 2013), the value of $\lambda_{\min}$ corresponds to the largest cloud that needs to be parameterized. When the model grid spacing approaches the convection-permitting scale, some large deep convective clouds can be explicitly resolved, and $\lambda_{\min}$ should increase accordingly for scale-aware purpose. Given that the probability for entrainment rate between 0 and 0.1η is below 0.1%, which is almost negligible, here we set $\lambda_{\min} = 0.1\eta$ km^{-1} for the experiments performed in this study that are all configured with a resolution of 2 degrees (see section 3). Then, the mass flux of deep convection can be obtained from Eq. 2 once we know the mass flux associated with shallow convection derived from the distribution of vertical velocity (w) primarily provided by CLUBB:

$$M_{\text{shallow}}(z_{\text{LCL}}) = \rho \int_{w_{\min}}^{+\infty} w \cdot g(w) dw, \quad (3)$$

where $w_{\min} = 0.1$ m s^{-1} is the threshold of vertical velocity for shallow convection. Lu et al. (2012) found that changing the threshold from 0.0 m s^{-1} to 0.5 m s^{-1} has only a weak impact on the estimated entrainment rate. $g(w)$ is the probability density function of w at LCL. In CLUBB, w follows a double Gaussian distribution, which is skewed to the higher values of w when shallow convection is present, complicating the calculation of Eq. 3. For convenience, we treat $g(w)$ as a normal distribution with its standard deviation determined by both the sub-grid information in CLUBB and the cold pool effects from deep convection (see section 2.2).

In the original ZM scheme, the minimum entrainment rate for deep convection is zero and the mass flux of the updraft cloud ensemble at each level (z) is formulated as:

$$M_{\text{deep}}(z) = M_{\text{deep}}(z_b) \int_0^{\lambda_D(z)} \frac{1}{\lambda_0} e^{\lambda(z-z_b)} d\lambda, \quad (4)$$

This article is protected by copyright. All rights reserved.

Accepted Article

where z_b is the height of the convection launch layer and $\lambda_D(z)$ is the entrainment rate corresponding to the plume that detrains at height z. Given that the minimum entrainment rate is set to $\lambda_{\min}$ in the new closure, we update Eq. 4 as:

$$M_{\text{deep}}(z) = M_{\text{deep}}(z_b) \int_{\lambda_{\min}}^{\lambda_D(z)} \frac{1}{\lambda_0 - \lambda_{\min}} e^{\lambda(z-z_b)} d\lambda$$

$$= \left(\frac{M_{\text{deep}}(z_b)}{(\lambda_0 - \lambda_{\min})(z-z_b)}\right)\left(\exp\left(\lambda_D(z)(z-z_b)\right) - \exp\left(\lambda_{\min}(z)(z-z_b)\right)\right). \quad (5)$$

Note that in the original ZM scheme, mass flux at the convection launch layer, i.e., $M_{\text{deep}}(z_b)$, is directly computed based on CAPE, while in the revised scheme, $M_{\text{deep}}(z_b)$ is calculated from $M_{\text{deep}}(z_{\text{LCL}})$ (in Eq. 2) based on the vertical profile of mass flux (i.e., Eq. 5).

2.2 Impacts of convection feedback

Convection has its own memory. Idealized cloud-resolving model simulations by Colin et al. (2019) revealed that the spatial variability in water vapor and temperature, especially in the lower troposphere induced by convection can affect convection in the following 2-3 h (24 h) for unorganized (organized) cases. By contrast, the impacts of hydrometeors or winds are much weaker. Precipitation itself has negligible memory and removing in-cloud hydrometeor information in the model has very weak effect on the upcoming convection. However, surface precipitation rate can be used as an effective indicator of convection intensity, convective cloud size, as well as interactions among multiple processes that are potentially related to convection memory, such as the evaporation-driven cold pool and spatial variability in water vapor and moist static energy. For example, Harrop et al. (2018) parameterized the effects of convective gustiness as a function of surface convective precipitation rate. Mapes and Neale (2011) used precipitation evaporation as a source for convection organization. In this study, we use the surface deep convective precipitation

This article is protected by copyright. All rights reserved.

rate (P_d) from the previous time step to parameterize the deep convection memory (A):

$$\frac{\partial A}{\partial t} = \alpha \cdot P_d - \frac{A}{\tau}. \quad (6)$$

The first and second terms on the right-hand-side of Eq. 6 represent the production and dissipation rates of A, respectively. Here, τ is set to 7200 s, close to the recovery time of 2-3 h in Colin (2019) for unorganized convection. The value of A is carried over time but reset to 0 when its value is below 0.05. We set α=2/3 mm^{-1}. Given that the ratio of global mean precipitation to precipitation evaporation is approximately 3:1, the generation rate of A in Eq. 6 is comparable to that parameterized by Mapes & Neale (2011), in which the increase of the organization degree per unit of evaporation is 2 mm^{-1}. However, it is more suitable to consider A in Eq. 6 as an index for the maturity of individual convective cells rather than organization at the mesoscale, which generally represents the spatial aggregation of convective cells and is accompanied by remarkable contrasts between moist and dry regions in a model grid point.

In this study, A can affect deep convection in two ways. First, cloud size (or radius), which can increase with the development of convection, is a key factor governing the width of the entrainment distribution η (in Eq. 1). Here we let cloud radius increase by a factor of a when A (in Eq. 6) increases from 0 to 1, which further leads to decreased entrainment rate (Kain, 2004; de Rooy et al., 2013). We set $a = 0.5$, producing a relative change in cloud radius half of that applied in the Kain–Fritsch convective parameterization, which uses a range of 1–2 km for cloud radius (Kain, 2004). However, one can image that when shallow cumuli dominate, they rarely produce surface precipitation (that is used to parameterize A) but can still grow horizontally as shallow convection develops, further increasing the probability for convective plumes extending above z_0 (corresponding to the shallowest plume in ZM). To consider this process, η is allowed to vary with

This article is protected by copyright. All rights reserved.

the ratio of water vapor flux of shallow convection at z_0 to that at LCL, i.e., $\mathrm{QFX}_{z_0}/\mathrm{QFX}_{\mathrm{lcl}}$ provided by CLUBB. This vertical-scale ratio can approximately reflect the changes in the shallow plume width because larger clouds sampled at LCL will more likely reach the level of z_0, with a higher $\mathrm{QFX}_{z_0}/\mathrm{QFX}_{\mathrm{lcl}}$ due to weaker dilution from entrainment. The above assumption is similar to that applied in the MYNN (i.e., Mellor–Yamada–Nakanishi–Niino)–EDMF scheme (Olson et al., 2019), which also links the shallow plume widths to a vertical scale, i.e., the boundary-layer height. As deep convective clouds start to rain, the entrainment distribution should become more dependent on the characteristics of deep convection (i.e., A in this study). Finally, the evolution of η is given by:

$$\eta = \eta_0 \min\left(\frac{1}{1+aA}, \frac{\mathrm{QFX}_{\mathrm{lcl}}}{b \cdot \mathrm{QFX}_{z_0}}\right), \tag{7}$$

where b is a tunable parameter and is set to 2 in this study. It indicates that η is determined by the smaller one of the two terms on the right-hand side of Eq. 7 to reflect the different roles of shallow and deep convection at different stages. η_0 represents the value of η when convection just starts, the impacts of which will be discussed in section 4.1.

Second, as deep convection develops, the evaporation of precipitation can drive cold pool that further enhances the spatial variability of the upward velocity w. This is mainly because of the increased boundary-layer inhomogeneities in temperature (Mapes and Neale, 2011) and secondary updrafts due to strong outflows associated with the gust front (Feng et al., 2015), both of which can be assumed to rise in proportion to convection memory or surface precipitation rate (Mapes and Neale, 2011; Harrop et al., 2018). The impact of cold pool on the standard deviation of w at LCL (i.e. σ_{wlcl}) is formulated as:

$$\sigma_{\mathrm{wlcl}} = \sqrt{{\sigma_{\mathrm{clubb}}}^2 + {\sigma_{\mathrm{cold_pool}}}^2}, \tag{8}$$

This article is protected by copyright. All rights reserved.

Accepted Article

where σ_{clubb} is the standard deviation of w provided by CLUBB and $\sigma_{\text{cold_pool}}$ is that contributed by cold pool, which is parameterized as $A \cdot \sigma_0$. We set σ_0 to 0.5 m s^{-1}, with its magnitude comparable to the daily-maximum value of σ_{clubb}.

2.3 Unrestricted launch level for deep convection

In the original ZM parameterization, the launch level of deep convection is restricted within the boundary layer. However, earlier studies suggested that nocturnal convection is often elevated, with the most unstable air located above the boundary layer and the launch level decoupled from the surface over the US Great Plains (Geerts et al., 2017; Marsham et al., 2011; Xie et al., 2014). Wang et al. (2015) and Xie et al. (2019) found that using an unrestricted launch level (ULL) trigger that allows the convective updrafts to be launched above the boundary layer can greatly improve the simulations of nocturnal convection.

In this study, we follow the ULL concept in the revised ZM scheme that searches the convection launch level within the lowest 400 hPa above the surface rather than in the boundary layer.

3 Experiments, data, and methods

3.1 Experimental design

We use the CESM version 1.2.1 with the Community Atmosphere Model version 5 (CAM5) model physics (Neale et al., 2010). The PBL turbulence, shallow convection, and macrophysics are represented by CLUBB (Bogenschutz et al., 2013). First, two SCM cases (ARM95 and TWP06) are selected to test the performance of the revised ZM scheme. The large-scale forcing data for the SCM experiments are derived from the CESM input repository (https://svn-ccsm-inputdata.cgd.ucar.edu/trunk/inputdata/atm/cam/scam/iop/), containing meteorological fields

This article is protected by copyright. All rights reserved.

Accepted Article

collected during two Intensive Observation Periods (IOPs) at the SGP site (262.5°E, 36.6°N) from 18 July to 3 August 1995 and at the Tropical western Pacific (TWP) site (130.891°E, 12.425°S) from 17 January to 12 February 2006. For each case, we conduct three experiments (i.e. CTL_ARM95/REV1_ARM95/REV2_ARM95 for the ARM95 case and CTL_TWP06/ REV1_TWP06/REV2_TWP06 for the TWP06 case; see Table 1). Taking the ARM95 case as an example, CTL_ ARM95 uses the original ZM scheme, while both REV1_ ARM95 and REV2_ ARM95 use the revised ZM scheme but with the parameter η_0 (eq. 7) set to 1 and 0.5, respectively.

Then, two GCM experiments (i.e., CTL and REV; Table 2) are conducted, which use the original and revised ZM scheme, respectively. Different from the SCM experiments, we set $\eta_0 = 0.5$ over land and $\eta_0 = 1$ over oceans in the GCM experiment with the revised scheme (i.e., REV). The reason is explained in section 4.1. We also conduct two additional GCM experiments, i.e. REV_ULL0 and REV_CF0. In REV_ULL0, the revised ZM scheme is used except that the convection launch level is still searched within the boundary layer. In REV_CF0, the value of *A* (Eq. 6) is always set to zero, so as to isolate the effects of the revised mass-flux closure from that of the deep convection feedback. To make the averaged entrainment rate and thus the convection intensity comparable to that in REV, in REV_CF0 we set $\eta_0 = 3/8$ over land and $\eta_0 = 3/4$ over oceans, both of which are in the varying range of η in REV. All the GCM experiments are run for 11 years forced by the observed climatological-mean monthly sea surface temperature (SST), with the last 10 years used for the analyses. The model is configured with a horizontal resolution of 2.5° longitude×1.9° latitude and 30 vertical hybrid levels.

3.2 Observational datasets

This article is protected by copyright. All rights reserved.

Accepted Article

The Tropical Rainfall Measuring Mission (TRMM; Huffman et al., 2007) 3B42 version 7 (available at ftp://disc2.nascom.nasa.gov/data/TRMM/Gridded) precipitation data from 2001 to 2010 are used for model evaluation on various scales. The TRMM data has a grid spacing of 0.25 degree with at a 3-h interval. The daily precipitation data from the Global Precipitation Climatology Project (GPCP; Adler et al., 2003) is used to evaluate the simulated MJO precipitation. In addition, the hourly rain-gauge data from the National Meteorological Information Center of China Meteorological Administration is used for evaluating the precipitation diurnal cycle simulation over China.

3.3 Analysis method

All of the observational data are interpolated onto the model grids using bilinear interpolation before comparisons. At each grid point, the intraseasonal component of precipitation associated with MJO is derived via a band□pass filter of 20–90 days.

When evaluating the simulated precipitation diurnal variation, precipitation at each hour of a day (i.e., $P(h)$) is normalized by the daily-mean precipitation (i.e., P_{mean}):

$$N(h) = \frac{P(h)-P_{\mathrm{mean}}}{P_{\mathrm{mean}}}, \quad (9)$$

where $N(h)$ is the normalized hourly precipitation.

4 Results

4.1 Precipitation simulations in SCM

In this subsection, we briefly evaluate the performance of the revised scheme during the two IOPs of ARM95 and TWP06. The observed and simulated time series of precipitation are given in

This article is protected by copyright. All rights reserved.

Accepted Article

Fig. 2. For both the ARM95 and TWP06 cases (top and bottom columns in Fig. 2, respectively), the simulations with the original ZM scheme (red lines) can capture the main precipitation events as in the observations (black lines) although some apparent model biases exist. The simulated precipitation using the revised scheme (with $\eta_0 = 1$) (blue lines) is slightly different from that using the default scheme, but the overall model skills with the two schemes are comparable with each other. Meanwhile, both of the two schemes can realistically capture the vertical distributions of the total diabatic heating associated with precipitation (Figs. S1 and S2), with strong heating rate at levels from 700 to 200 hPa during periods when strong precipitation events are present.

In the revised scheme, η_0 governs the overall strength of the convective entrainment. We find that in the two selected SCM cases, adjusting the value of η_0 from 1 to 0.5 has a weak effect on the precipitation simulations based on the time series (Fig. S3). Figure 3 shows the observed and simulated diurnal variations of precipitation averaged during the IOP of ARM95. We can see that the observed precipitation (black line) peaks at 15 Local Solar Time (LST). By contrast, the experiment with the original scheme produces two peaks at 13LST and 20LST (red line), respectively, with the first peak mainly contributed by convective precipitation (figure not shown) (because the CAPE-type closure often simulates a too-early onset of convection; Zhang, 2002). When using the revised scheme, the simulated precipitation (blue lines) peaks at around 18LST, later than that in observation. Decreasing the value of η_0 from 1.0 (blue dashed line) to 0.5 (blue solid line) tends to make convection initiate earlier.

In Fig. 4 we examine the impacts of η_0 on the diurnal variations of several elements related to convection memory, including the ratio of water vapor fluxes $\frac{\mathrm{QFX}_{z_0}}{\mathrm{QFX}_{\mathrm{lcl}}}$ (Eq. 7), deep convection memory (i.e., A in Eq. 6), the scaling factor for entrainment rate (i.e., η/η_0 in Eq. 7), and the

This article is protected by copyright. All rights reserved.

maximum entrainment rate assigned to deep convection (i.e., λ_0 in Eq. 2). The results are generally consistent between the two experiments with different values of η_0, except that the diurnal variations in η/η_0 (blue line) and *A* (red line) are stronger when a lower value of η_0 is applied (Fig. 4b). It shows that *A* increases with precipitation after 14LST (Fig. 3), although λ_0 (green line in Fig. 4) decreases during this period that is not favorable for the development of deep convection (based on Eq. 2). Hence, the increased *A* is mainly due to the enhanced shallow convective mass flux (based on Eq. 2; figure not shown) and larger $\frac{\mathrm{QFX}_{z_0}}{\mathrm{QFX}_{\mathrm{lcl}}}$ (black line in Fig. 4) that acts to decrease η (based on Eq. 7). Improving the representation of the evolution of η (i.e., Eq. 7) along with parameter optimization might improve the simulation of the precipitation diurnal cycle.

Different from the SCM results, GCM simulations indicate that convective precipitation is often too weak (strong) over the tropical land (oceans) when $\eta_0 = 1$ ($\eta_0 = 0.5$) (Fig. S4), indicating that we cannot simultaneously improve the convective precipitation simulation over the tropical land and oceans with a globally uniform value of η_0. This might be because η_0 is dependent on the background meteorological conditions, such as the upward velocity variability at LCL, atmosphere instability, and so on. At this stage, we set $\eta_0 = 0.5$ over land and $\eta_0 = 1$ over oceans in the GCM experiment REV (Table 2). In the following subsections, the analyses are mainly based on the GCM experiments.

4.2 Precipitation climatology

In Fig. 5 we evaluate the annual mean precipitation from simulations (averaged over the last 10 years) with different convective schemes against the TRMM observation (2001-2010). Compared to the TRMM result (Fig. 5a), clear biases are seen in the CTL experiment with the

This article is protected by copyright. All rights reserved.

Accepted Article

Accepted Article

original scheme (Fig. 5b), such as the underestimated precipitation over the TWP and the Bay of Bengal (BOB), as well as the overestimated precipitation over the southeastern Pacific (i.e., the double-ITCZ problem). Over East Asia, the CTL experiment underestimates the midlatitude storm track precipitation over oceans to the south and east of Japan. Meanwhile, it underestimates (overestimates) the precipitation over the southern coastal (inland) regions of China, failing to capture the south to north and coastal to inland pattern of decreasing precipitation there. In the REV experiment with the revised scheme (Fig. 5c), the above precipitation biases are all reduced to some degree, making the precipitation simulations agree more with the observation in terms of both magnitude and spatial pattern in many regions. For example, the double-ITCZ problem is less obvious, which can also be clearly seen in the meridional distribution of precipitation averaged over the eastern Pacific (160ºW–90ºW) (Fig. 6). However, the northern ITCZ is overestimated by using the revised closure (blue line in Fig. 6). When turning off the ULL option in the revised scheme (i.e. the REV_ULL0 experiment), the results (Fig. 5d) are generally consistent with those in REV, suggesting that the improved precipitation climatology in REV compared to that in CTL is mainly due to the modifications related to the mass-flux closure and the convection feedback effects, with the two individual impacts discussed in section 4.6.

We further compare the simulated precipitation averaged in June-July-August (JJA) and December-January-February (DJF) against the observation (Fig. 7). In JJA, large precipitation amounts are observed over the BOB, eastern equatorial Indian Ocean (EIO), northern-ITCZ, and TWP (Fig. 7a). There exists a clear rain-belt from China to Japan, which is associated with the East Asian summer monsoon (EASM). The CTL experiment (Fig. 7c) fails to capture the strong precipitation over the TWP, with the rainfall center shifted southward to the Maritime Continent

This article is protected by copyright. All rights reserved.

Accepted Article

compared to the observation. Meanwhile, the EASM precipitation is too weak. In addition, the CTL experiment underestimates (overestimates) the precipitation over the eastern (western) EIO, exhibiting an Indian Ocean dipole-like bias that is also seen in many other GCMs (Li et al., 2015). The REV experiment with the revised scheme better simulates the precipitation distribution over the broad western Pacific region, including the EASM region, Maritime Continent, and TWP (Fig. 7e). However, the underestimated precipitation over the eastern EIO becomes more apparent which deserves further investigations.

In DJF, large precipitation amounts are observed over the Maritime Continent, the northern-ITCZ, and the South Pacific Convergence Zone (SPCZ) (Fig. 7b). A strong rainfall center is also seen in the Amazon region. The CTL experiment underestimates the SPCZ precipitation, especially in the areas to the east of Australia (Fig. 7d). This bias is alleviated to some extent in the REV experiment (Fig. 7f).

Overall, the above results indicate that the revised ZM scheme can realistically capture the main features in the mean state of precipitation and perform better than the original scheme in many aspects.

4.3 Seasonal variation of precipitation

Rainfall centers experience strong south-north oscillation following the seasonal variation in SST that is primarily driven by the solar radiation. Previous studies revealed that the strength of the double ITCZ varies with seasons (Zhang et al. 2019). Figure 8 shows the month-latitude distributions of precipitation over the eastern Pacific (160ºW-90ºW) in both the TRMM observation and simulations. In the observation (Fig. 8a), the main rain-belt in the northern ITCZ is situated

This article is protected by copyright. All rights reserved.

Accepted Article

around 8ºN and reaches its northernmost and southernmost location in September and March, respectively. Compared to the northern component, the precipitation in the southern oceans is much weaker, with its maximum magnitude around 4 mm day^{-1} from March to April. The CTL experiment (Fig. 8b) can reasonably simulate the seasonal variation of precipitation in the northern ITCZ, but largely overestimates the southern ITCZ precipitation in March and April, consistent with the results shown in Figs. 5 and 6. By contrast, the intensity of the southern ITCZ is markedly reduced in the REV experiment (Fig. 8c). The result from REV_ULL0 is not presented here because it is largely consistent with that from REV.

The seasonal migration of precipitation is a prominent phenomenon over the monsoon regions. Around the globe, East Asia is a distinct region where the precipitation climate is dominated by the evolution of monsoon. Figure 9 presents the month-latitude distributions of precipitation over East Asia and its adjacent ocean areas (105ºE-130ºE). In the observation (Fig. 9a), the precipitation maximum is located south of the equator from December to April and gradually migrated to 20ºN from May to August, corresponding to the onset of the Western North Pacific summer monsoon. Then, it retreats back to the south. A separate rain-belt forms in May between 20ºN and 30ºN and extends to 40ºN in July and August, corresponding to the northward advance of the EASM precipitation. The CTL experiment (Fig. 9b) produces large biases in the seasonal variation of precipitation over East Asia, especially to the south of 20ºN. For example, the precipitation maximum is always located around the equator throughout the year, consistent with the too weak precipitation over TWP in JJA (Fig. 7c). Meanwhile, the EASM precipitation is largely underestimated, particularly in July and August. In contrast, the REV experiment (Fig. 9c) can well capture the seasonal variation of precipitation in the tropical oceans and better simulate the EASM

This article is protected by copyright. All rights reserved.

precipitation in terms of both mean magnitude and seasonal migration.

4.4 The MJO precipitation

Figure 10 shows the time lag–longitude distributions of correlation coefficients of the intraseasonal component of precipitation averaged from 10°S to 10°N with that averaged in two reference regions, i.e. the Indian Ocean region (70°E–90°E, 5°S–5°N; left column of Fig. 10) and the western Pacific Ocean (130°E–150°E, 5°S–5°N; right column of Fig. 10), which are often applied to characterize the MJO activity (e.g., Boyle et al. 2015). The plots are derived based on the precipitation data from November to April when the MJO activity is the most prominent. In the observation (Figs. 10a and 10b), we can see a notable eastward propagation of the MJO precipitation anomaly from Indian Ocean to the western Pacific Ocean. However, the CTL experiment (Figs. 10c and 10d) simulates a westward propagation of the precipitation anomalies, opposite to that in the observation. The MJO simulation in REV (Figs. 10e and 10f) is improved to some degree compared to that in CTL, although the eastward propagation is still less obvious than in the observation. We consider that the low skill of the MJO simulation in CTL is largely because convection often occurs too easily in the original ZM scheme. Previous studies have shown that tuning several key parameters in the convective scheme can considerably improve the MJO simulation (Boyle et al. 2015; Liu et al. 2019). Our preliminary test experiments also indicate that the MJO simulation in REV can be further improved when the overall intensity of convection is suppressed via using a different value for η_0 or a in Eq. 7.

4.5 Precipitation diurnal variation

Many previous studies have demonstrated the important roles of the transition from shallow to

This article is protected by copyright. All rights reserved.

Accepted Article

deep convection in regulating the precipitation diurnal variations (Rio et al. 2009; Yang et al. 2020). Figure 11 shows the spatial patterns of the diurnal peak time (i.e. the hour corresponding to the daily-maximum precipitation) for the annual mean precipitation in the TRMM observation and different simulations. In the TRMM (Fig. 11a), precipitation often peaks at around 17LST over land, except for some subtropical and midlatitude areas, such as those adjacent to the Tibetan Plateau (TP) over East Asia and east of Rocky Mountains over North America, where nighttime precipitation maximum can be observed as revealed in previous studies (e.g., Dai et al., 1999). Over oceans, precipitation generally peaks during nighttime or early morning.

All the simulations with different convective schemes can well capture the nighttime precipitation peaks over oceans as in the observation (Figs. 11b-11d). However, large biases and inter-model differences are found over land. In the CTL experiment (Fig. 11b), precipitation over tropical land often shows noontime diurnal peaks, which are much earlier than that in the observation. Meanwhile, the CTL experiment fails to produce the nighttime precipitation peak over regions east of TP or Rocky Mountains.

In the REV experiment (Fig. 11c), adopting the revised scheme improves the simulations of the precipitation diurnal features over many tropical land regions, with the peak time delayed from 12LST to around 15LST which is still about 2-3h earlier than that in the observation. Moreover, the revised scheme can reproduce the nighttime peaks of precipitation over East Asia and North America. However, the areas with nighttime peaks are much wider than in the observation. In the REV_ULL0 experiment with the ULL option turned off (Fig. 11d), the nighttime precipitation peaks are still clearly seen over East Asia and North America but the associated areas are largely reduced compared to the REV simulations. However, the simulated diurnal peaks over the tropical land are

This article is protected by copyright. All rights reserved.

Accepted Article

too early, similar to that in CTL. These results indicate that both the ULL configuration and the modifications related to the mass-flux closure and convection feedback impacts can affect the simulations of the precipitation diurnal variations.

We further evaluate the simulated diurnal variations of the summertime mean (i.e. JJA) precipitation over the US (Fig. 12), which is usually hard to represent by the traditional convective parameterizations (Xie et al., 2019). In the TRMM (Fig. 12a), precipitation is featured by late-afternoon diurnal peaks over the western and southeastern parts of the US and nighttime peaks over the Great Plains, exhibiting a propagating feature of the diurnal peak time east of Rocky Mountains. The CTL experiment with the original ZM scheme (Fig. 12b) well captures the late-afternoon precipitation peaks over the western and southeastern regions but fails to simulate the nighttime peaks over the Great Plains. By contrast, in the REV experiment with the revised scheme (Fig. 12c), the spatial distribution of the diurnal peak time is improved to a large degree. In REV_ULL0 (Fig. 12d), the nighttime peak is also seen but only over a limited region east of Rocky Mountains. We also conduct a 11-year experiment using the original ZM scheme but with the ULL option turned on, in which the nighttime diurnal peaks are better simulated but still weaker than in the TRMM (figure not shown). These results confirm that different modifications to the ZM scheme can individually affect the simulation of the precipitation diurnal variation over this region.

Figure 13 further illustrates the propagating feature of the diurnal peak time of precipitation (normalized value based on Eq. 9) over the areas east of Rocky Mountains. In the TRMM (Fig. 13a), precipitation shows a strong diurnal peak at around 18LST over Rocky Mountains (i.e., west of 105°W). To the east (i.e., 105°W-90°W), the diurnal peak time gradually shifts from late afternoon (i.e. 18LST) to early morning (i.e. 05LST). The CTL experiment (Fig. 13b) fails to simulate the

This article is protected by copyright. All rights reserved.

Accepted Article

Accepted Article

propagation. By contrast, the REV experiment (Fig. 13c) with the revised scheme well captures such feature, consistent with the results shown in Fig. 12c. In REV_ULL0, the shift in the precipitation diurnal peak time is also partly reproduced but the propagation signal disappears at around 102°W.

In Fig. 14 we compare the simulated diurnal variations of precipitation over the EASM region against the TRMM and rain-gauge records. Previous studies have revealed that the EASM precipitation is characterized by complex diurnal features (Yu et al., 2007). The distributions of the diurnal peak time are different in the TRMM and in the rain-gauge records (Fig. 14a vs. Fig. 14e). For example, the rain-gauge precipitation over China is featured by late-afternoon peaks over the southeastern coastal areas and nighttime peaks over most inland areas to the south of 40°N. While in the TRMM, the nighttime precipitation peak is rarely seen to the east of 110°E. The convective scheme has strong impacts on the precipitation diurnal variation simulations over East Asia (Figs. 14b-14d). The CTL experiment (Fig. 14b) simulates a too early peak over southeastern China and fails to capture the nighttime peaks to the north. By contrast, the revised scheme (Fig. 14c) slightly delays the late afternoon peaks over southeastern China. It can also reproduce the nighttime peaks but over a much wider region than in the observations (Figs. 14a and 14e). The simulated precipitation diurnal features in REV_ULL0 are generally consistent with that in CTL, except that REV_ULL0 performs better in capturing the nighttime precipitation peaks over the Sichuan Basin (around 105°E and 30°N)

The simulated propagation of the precipitation diurnal feature east of TP is also compared against observations in Fig. 15. In both the TRMM (Fig. 15a) and rain-gauge records (Fig. 15e), the precipitation diurnal peak gradually shifts from around 20LST to 06LST downstream of TP (i.e., 100°E-110°E). As revealed previously (e.g., Yang et al., 2020), the original ZM scheme has

This article is protected by copyright. All rights reserved.

Accepted Article

difficulty in simulating the propagating feature and nighttime peaks along the regions east of TP (Fig. 15b). Notably, the REV experiment performs much better in this regard (Fig. 15c). The REV_ULL0 experiment can also well capture the propagating feature of the precipitation diurnal peak there (Fig. 15d).

4.6 Impacts of convection feedback

In the above subsections we have demonstrated the benefits of using the revised ZM scheme in simulating the mean state and variability of precipitation. However, it is unclear how the two modifications related to the mass-flux closure (i.e., section 2.1) and the convection feedback impacts (i.e., section 2.2) contribute to the improved model behaviors individually. Here, an additional experiment REV_CF0 with the convection feedback effects turned off is used to further understand the individual impacts of the two components. Figure 16 shows the annual mean precipitation distribution simulated in REV_CF0, which is generally consistent with that in REV (Fig. 5c) in terms of both magnitude and spatial pattern, except that the precipitation amount over Amazon is smaller in REV_CF0 than in REV. The precipitation distributions averaged in JJA and DJF are also largely consistent between the two simulations (Fig. S5 vs. Figs. 7e and 7f), indicating that the improved mean state of precipitation in REV is mainly contributed by the modification related to the mass-flux closure.

Figure 17 shows the lag□longitude distributions of correlation coefficients of band-pass filtered (20-90 days) precipitation (averaged for 10°S-10°N) with precipitation averaged over the Indian Ocean region and the western Pacific region in REV_CF0. We can see that in REV_CF0 the simulated MJO precipitation is improved to a large degree compared to that in CTL (Figs. 10c and

This article is protected by copyright. All rights reserved.

10d) and even better than that in REV (Figs. 10e and 10f). We find that the overall convection intensity is weaker in REV_CF0 than in REV although a smaller value of η_0 is applied. The relatively weaker convection in REV_CF0 is likely responsible for the better-simulated MJO precipitation.

It has been suggested that the convection feedback impacts are of vital importance to the simulations of precipitation diurnal cycle across various climate regimes. In Fig. 18 we show the spatial distribution of the diurnal peak times for the JJA mean precipitation over the US simulated by REV_CF0. Notably, with the convection feedback impacts turned off, the model can still capture the nighttime peaks of precipitation downstream of Rocky Mountains and thus the propagating feature there. However, the simulated diurnal peaks are too early over the southeastern region of the US. Similarly, the REV_CF0 experiment also fails to capture the late-afternoon peaks of precipitation over southeastern China (Fig. S6) and over the tropical land (figure not shown), probably because the transition from shallow to deep convection is important there and the convection feedback impacts need to be explicitly or implicitly parameterized in climate models.

5 Summary and discussions

In this study, we modified the closure of the ZM convective parameterization in CAM5 and coupled it with CLUBB to provide a unified treatment for sub-grid vertical motions across regimes of boundary-layer turbulence, shallow convection and deep convection. Instead of using CAPE as a closure for the ZM scheme, by assuming a lognormal distribution to represent the spectrum of entrainment rates across the entire moist convective regimes, we link mass flux for deep convection to that of shallow convection, which is determined by the sub-grid information of vertical velocity

This article is protected by copyright. All rights reserved.

Accepted Article

Accepted Article

in CLUBB. The modified mass-flux closure improves the consistency between shallow and deep convection, as well as between the deep convective closure and updraft plumes in the ZM scheme. In addition, the convection feedback effects were considered to decrease the entrainment spectrum width and enhance the vertical velocity variability that further affect deep convection. We also included a ULL concept that allows the ZM scheme to search the convection launch level above the boundary-layer height so as to improve the precipitation diurnal variation.

First, the performance of the revised ZM scheme was evaluated with two SCM experiments, in which the simulated precipitation and associated atmospheric heating profiles are generally consistent with that using the original ZM scheme and with the observation. Then, we focused on the global simulations of precipitation in terms of the mean state and variability at various timescales. The revised scheme greatly improves the precipitation climatology, such as the alleviated double-ITCZ problem, and better-simulated south-north distributions of precipitation over the TWP and East Asia. Meanwhile, the seasonal variations of precipitation associated with the Western North Pacific summer monsoon and EASM are improved to a large degree. The MJO precipitation is also improved by using the revised scheme.

The revised scheme can considerably improve the precipitation diurnal variations over land. For example, the diurnal peak time of precipitation is delayed from 12LST to around 15LST, in better agreement with the observation (i.e. 17LST). Meanwhile, the revised scheme can realistically capture the propagating features of the precipitation diurnal variation downstream of TP and Rocky Mountains. When turning off the ULL option in the revised scheme, the model fails to capture the late-afternoon precipitation peaks over the tropical land, but still shows some skills in simulating the propagating features downstream of TP and Rocky Mountains, indicating that both the ULL

This article is protected by copyright. All rights reserved.

Accepted Article

configuration and the modifications related to the mass-flux closure and the convection feedback impacts can affect the precipitation diurnal variation simulations.

An additional experiment turning off the convection feedback effects was conducted to investigate how the modified mass-flux closure and the convection feedbacks contribute to the improved model behaviors individually. It showed that without the convection feedback impacts the improvements can still be seen in many aspects, such as the better-simulated precipitation climatology, MJO, and nighttime precipitation diurnal peaks downstream of Rocky Mountains, emphasizing the benefits of using the revised mass-flux closure. However, the simulated diurnal peaks are often too early over regions with late-afternoon precipitation peaks, likely because the convection feedback impacts are important for the gradual transition from shallow to deep convection over these regions.

Overall, in this study we proposed to modify the ZM scheme that couples deep convection to shallow convection based on the sub-grid information in CLUBB, which helps improve the consistency between shallow and deep convection. The convection feedback impacts were also considered but large uncertainty is expected in the formulations (Colin et al. 2019). Further studies are needed to better characterize such effects using high-resolution model simulations. In addition, the organization of convection at the mesoscale was not included, which could potentially be parameterized via using the sub-grid atmospheric variability (i.e. humidity contrast between moist and dry regions) provided by CLUBB or produced by convection itself (e.g. Wing et al. 2017).

Acknowledgments

This article is protected by copyright. All rights reserved.

Accepted Article

This work is jointly supported by the National Natural Science Foundation of China (41675101), National key research and development program (2017YFA0604002), and Jiangsu Collaborative Innovation Center of Climate Change. We thank Xin Xu and Dejian Yang for discussions about the PDF integrations, and Zeyu Cui and Yong Wang for discussions about setting up SCM. Two anonymous reviewers are thanked for their constructive comments. Guang Zhang is supported by the Department of Energy Office of Science, Biological and Environmental Research Program (BER) under Award Number DE-SC0019373. The contribution of Yun Qian in this study is supported by the U.S. Department of Energy's Office of Science as part of the Atmospheric System Research (ASR) program. The Pacific Northwest National Laboratory is operated for DOE by Battelle Memorial Institute under contract DE-AC05-76RL01830. The numerical calculations in this paper have been done on the computing facilities in the High Performance Computing Center (HPCC) of Nanjing University. The model outputs and observational data used in this study are publicly available from Zenodo (https://doi.org/10.5281/zenodo.4059170). All the graphics in this study are created by the NCAR Command Language (NCL; doi:10.5065/D6WD3XH5).

Reference

Adler, R. F., Huffman, G. J., Chang, A., Ferraro, R., Xie, P. P., Janowiak, J., et al. (2003). The version-2 global precipitation climatology project (GPCP) monthly precipitation analysis (1979-present). *Journal of Hydrometeorology, 4*(6), 1147-1167. https://doi.org/Doi 10.1175/1525-7541(2003)004<1147:Tvgpcp>2.0.Co;2

Arakawa, A. (2004). The Cumulus Parameterization Problem: Past, Present, and Future. *Journal*

This article is protected by copyright. All rights reserved.

Accepted Article

of Climate, 17(13), 2493-2525. https://doi.org/10.1175/1520-0442(2004)017<2493:Ratcpp>2.0.Co;2

Arakawa, A., & Schubert, W. H. (1974). Interaction of a Cumulus Cloud Ensemble with Large-Scale Environment .1. *Journal of the Atmospheric Sciences, 31*(3), 674-701. https://doi.org/Doi 10.1175/1520-0469(1974)031<0674:Ioacce>2.0.Co;2

Bechtold, P., Semane, N., Lopez, P., Chaboureau, J. P., Beljaars, A., & Bormann, N. (2014). Representing Equilibrium and Nonequilibrium Convection in Large-Scale Models. *Journal of the Atmospheric Sciences, 71*(2), 734-753. https://doi.org/10.1175/Jas-D-13-0163.1

Bogenschutz, P. A., Gettelman, A., Morrison, H., Larson, V. E., Craig, C., & Schanen, D. P. (2013). Higher-Order Turbulence Closure and Its Impact on Climate Simulations in the Community Atmosphere Model. *Journal of Climate, 26*(23), 9655-9676. https://doi.org/10.1175/jcli-d-13-00075.1

Boyle, J. S., Klein, S. A., Lucas, D. D., Ma, H. Y., Tannahill, J., & Xie, S. (2015). The parametric sensitivity of CAM5's MJO. *Journal of Geophysical Research: Atmospheres, 120*(4), 1424-1444. https://doi.org/10.1002/2014jd022507

Colin, M., Sherwood, S., Geoffroy, O., Bony, S., & Fuchs, D. (2019). Identifying the Sources of Convective Memory in Cloud-Resolving Simulations. *Journal of the Atmospheric Sciences, 76*(3), 947-962. https://doi.org/10.1175/jas-d-18-0036.1

Dai, A. (1999). Recent changes in the diurnal cycle of precipitation over the United States. *Geophysical Research Letters, 26*(3), 341-344. https://doi.org/10.1029/1998gl900318

de Rooy, W. C., Bechtold, P., Fröhlich, K., Hohenegger, C., Jonker, H., Mironov, D., et al. (2013).

This article is protected by copyright. All rights reserved.

Accepted Article

Entrainment and detrainment in cumulus convection: an overview. Quarterly Journal of the Royal Meteorological Society, 139(670), 1-19. https://doi.org/10.1002/qj.1959

Dirmeyer, P. A., Cash, B. A., Kinter, J. L., Jung, T., Marx, L., Satoh, M., et al. (2012). Simulating the diurnal cycle of rainfall in global climate models: resolution versus parameterization. *Climate Dynamics, 39*(1-2), 399-418. https://doi.org/10.1007/s00382-011-1127-9

Emanuel, K. (2020). The Relevance of Theory for Contemporary Research in Atmospheres, Oceans, and Climate. *AGU Advances, 1*(2). https://doi.org/10.1029/2019av000129

Emanuel, K. A., & Zivkovic-Rothman, M. (1999). Development and evaluation of a convection scheme for use in climate models. *Journal of the Atmospheric Sciences, 56*(11), 1766-1782. https://doi.org/Doi 10.1175/1520-0469(1999)056<1766:Daeoac>2.0.Co;2

Eyring, V., Bony, S., Meehl, G. A., Senior, C. A., Stevens, B., Stouffer, R. J., & Taylor, K. E. (2016). Overview of the Coupled Model Intercomparison Project Phase 6 (CMIP6) experimental design and organization. *Geoscientific Model Development, 9*(5), 1937-1958. https://doi.org/10.5194/gmd-9-1937-2016

Feng, Z., Hagos, S., Rowe, A. K., Burleyson, C. D., Martini, M. N., & Szoeke, S. P. (2015). Mechanisms of convective cloud organization by cold pools over tropical warm ocean during the AMIE/DYNAMO field campaign. Journal of Advances in Modeling Earth Systems, 7(2), 357-381. https://doi.org/10.1002/2014ms000384

Fuchs, Z., & Raymond, D. J. (2007). A simple, vertically resolved model of tropical disturbances with a humidity closure. *Tellus Series a-Dynamic Meteorology and Oceanography, 59*(3), 344-354. https://doi.org/10.1111/j.1600-0870.2007.00230.x

Geerts, B., Parsons, D., Ziegler, C. L., Weckwerth, T. M., Biggerstaff, M. I., Clark, R. D., et al.

This article is protected by copyright. All rights reserved.

Accepted Article

(2017). The 2015 Plains Elevated Convection at Night Field Project. *Bulletin of the American Meteorological Society, 98*(4), 767-786. https://doi.org/10.1175/Bams-D-15-00257.1

Golaz, J. C., Larson, V. E., & Cotton, W. R. (2002). A PDF-based model for boundary layer clouds. Part I: Method and model description. *Journal of the Atmospheric Sciences, 59*(24), 3540-3551. https://doi.org/Doi 10.1175/1520-0469(2002)059<3540:Apbmfb>2.0.Co;2

Grabowski, W. W. (2001). Coupling cloud processes with the large-scale dynamics using the Cloud-Resolving Convection Parameterization (CRCP). *Journal of the Atmospheric Sciences, 58*(9), 978-997. https://doi.org/Doi 10.1175/1520-0469(2001)058<0978:Ccpwtl>2.0.Co;2

Grell, G. A., & Devenyi, D. (2002). A generalized approach to parameterizing convection combining ensemble and data assimilation techniques. *Geophysical Research Letters, 29*(14), 1693. https://doi.org/10.1029/2002gl015311

Guo, X., Lu, C., Zhao, T., Zhang, G., & Liu, Y. (2015). An Observational Study of Entrainment Rate in Deep Convection. Atmosphere, 6(9), 1362-1376. https://doi.org/10.3390/atmos6091362

Hannah, W. M., Jones, C. R., Hillman, B. R., Norman, M. R., Bader, D. C., Taylor, M. A., et al. (2020). Initial Results From the Super- Parameterized E3SM. *Journal of Advances in Modeling Earth Systems, 12*(1). https://doi.org/10.1029/2019ms001863

Harrop, B. E., Ma, P. L., Rasch, P. J., Neale, R. B., & Hannay, C. (2018). The Role of Convective Gustiness in Reducing Seasonal Precipitation Biases in the Tropical West Pacific. Journal

This article is protected by copyright. All rights reserved.

Accepted Article

of Advances in Modeling Earth Systems, 10(4), 961-970. https://doi.org/10.1002/2017ms001157

Huffman, G. J., Adler, R. F., Bolvin, D. T., Gu, G. J., Nelkin, E. J., Bowman, K. P., et al. (2007). The TRMM multisatellite precipitation analysis (TMPA): Quasi-global, multiyear, combined-sensor precipitation estimates at fine scales. *Journal of Hydrometeorology, 8*(1), 38-55. https://doi.org/10.1175/Jhm560.1

Kain, J. S. (2004). The Kain-Fritsch convective parameterization: An update. Journal of Applied Meteorology, 43(1), 170-181. https://doi.org/10.1175/1520-0450(2004)043<0170:Tkcpau>2.0.Co;2

Kain, J. S., & Fritsch, J. M. (1990). A One-Dimensional Entraining Detraining Plume Model and Its Application in Convective Parameterization. *Journal of the Atmospheric Sciences, 47*(23), 2784-2802. https://doi.org/Doi 10.1175/1520-0469(1990)047<2784:Aodepm>2.0.Co;2

Khairoutdinov, M., Randall, D., & DeMott, C. (2005). Simulations of the atmospheric general circulation using a cloud-resolving model as a superparameterization of physical processes. *Journal of the Atmospheric Sciences, 62*(7), 2136-2154. https://doi.org/Doi 10.1175/Jas3453.1

Kooperman, G. J., Pritchard, M. S., & Somerville, R. C. J. (2013). Robustness and sensitivities of central US summer convection in the super-parameterized CAM: Multi-model intercomparison with a new regional EOF index. *Geophysical Research Letters, 40*(12), 3287-3291. https://doi.org/10.1002/grl.50597

Larson, V. E., & Golaz, J. C. (2005). Using probability density functions to derive consistent

This article is protected by copyright. All rights reserved.

Accepted Article

closure relationships among higher-order moments. *Monthly Weather Review, 133*(4), 1023-1042. https://doi.org/Doi 10.1175/Mwr2902.1

Li, G., Xie, S.-P., & Du, Y. (2015). Monsoon-Induced Biases of Climate Models over the Tropical Indian Ocean*. *Journal of Climate, 28*(8), 3058-3072. https://doi.org/10.1175/jcli-d-14-00740.1

Li, P., Furtado, K., Zhou, T., Chen, H., Li, J., Guo, Z., & Xiao, C. (2018). The diurnal cycle of East Asian summer monsoon precipitation simulated by the Met Office Unified Model at convection-permitting scales. *Climate Dynamics, 55*(1-2), 131-151. https://doi.org/10.1007/s00382-018-4368-z

Liu, X. W., Li, W. J., Wu, T. W., Li, T., Gu, W. Z., Bo, Z. K., et al. (2019). Validity of parameter optimization in improving MJO simulation and prediction using the sub-seasonal to seasonal forecast model of Beijing Climate Center. *Climate Dynamics, 52*(7-8), 3823-3843. https://doi.org/10.1007/s00382-018-4369-y

Lu, B., & Ren, H. L. (2016). Improving ENSO periodicity simulation by adjusting cumulus entrainment in BCC_CSMs. Dynamics of Atmospheres and Oceans, *76*, 127-140. https://doi.org/10.1016/j.dynatmoce.2016.10.005

Lu, C., Liu, Y., Niu, S., & Vogelmann, A. M. (2012). Lateral entrainment rate in shallow cumuli: Dependence on dry air sources and probability density functions. *Geophysical Research Letters, 39*(20). https://doi.org/10.1029/2012gl053646

Madden, R. A., & Julian, P. R. (1971), Detection of a 40–50 day oscillation in the zonal wind in the tropical pacific, J. Atmos. Sci., 28(5), 702–708, doi:10.1175/1520-0469(1971)028<0702:DOADOI>2.0.CO;2.

This article is protected by copyright. All rights reserved.

Accepted Article

Mapes, B., & Neale, R. (2011). Parameterizing Convective Organization to Escape the Entrainment Dilemma. *Journal of Advances in Modeling Earth Systems, 3*(2), n/a-n/a. https://doi.org/10.1029/2011ms000042

Marsham, J. H., Dixon, N. S., Garcia-Carreras, L., Lister, G. M. S., Parker, D. J., Knippertz, P., & Birch, C. E. (2013). The role of moist convection in the West African monsoon system: Insights from continental-scale convection-permitting simulations. *Geophysical Research Letters, 40*(9), 1843-1849. https://doi.org/10.1002/grl.50347

Marsham, J. H., Trier, S. B., Weckwerth, T. M., & Wilson, J. W. (2011). Observations of Elevated Convection Initiation Leading to a Surface-Based Squall Line during 13 June IHOP_2002. *Monthly Weather Review, 139*(1), 247-271. https://doi.org/10.1175/2010mwr3422.1

Neale, R. B., Richter, J. H., & Jochum, M. (2008). The Impact of Convection on ENSO: From a Delayed Oscillator to a Series of Events. Journal of Climate, *21*(22), 5904-5924. https://doi.org/10.1175/2008jcli2244.1

Neale, R. B., Gettelman, A., Park, S., Conley, A. J., Kinnison, D., Marsh, D., et al. (2010). Description of the NCAR Community Atmosphere Model (CAM5). NCAR Tech. Note NCAR/TN□4861STR (283 pp).

Olson, J. B., Kenyon, J. S., Angevine, W. A., Brown, J. M., Pagowski, M., & Sušelj, K. (2019). A Description of the MYNN-EDMF Scheme and the Coupling to Other Components in WRF-ARW. NOAA Technical Memorandum OAR GSD-61.

Park, S. (2014). A Unified Convection Scheme (UNICON). Part I: Formulation. *Journal of the*

This article is protected by copyright. All rights reserved.

Accepted Article

Atmospheric Sciences, 71(11), 3902-3930. https://doi.org/10.1175/jas-d-13-0233.1

Park, S. (2014). A Unified Convection Scheme (UNICON). Part II: Simulation. *Journal of the Atmospheric Sciences, 71*(11), 3931-3973. https://doi.org/10.1175/jas-d-13-0234.1

Piriou, J. M., Redelsperger, J. L., Geleyn, J. F., Lafore, J. P., & Guichard, F. (2007). An approach for convective parameterization with memory: Separating microphysics and transport in grid-scale equations. *Journal of the Atmospheric Sciences, 64*(11), 4127-4139. https://doi.org/10.1175/2007jas2144.1

Randall, D., Khairoutdinov, M., Arakawa, A., & Grabowski, W. (2003). Breaking the cloud parameterization deadlock. *Bulletin of the American Meteorological Society, 84*(11), 1547-1564. https://doi.org/10.1175/Bams-84-11-1547

Raymond, D. J. (1994). Convective Processes and Tropical Atmospheric Circulations. *Quarterly Journal of the Royal Meteorological Society, 120*(520), 1431-1455. https://doi.org/DOI 10.1256/smsqj.52001

Rio, C., Del Genio, A. D., & Hourdin, F. (2019). Ongoing Breakthroughs in Convective Parameterization. *Current Climate Change Reports, 5*(2), 95-111. https://doi.org/10.1007/s40641-019-00127-w

Rio, C., Hourdin, F., Grandpeix, J. Y., & Lafore, J. P. (2009). Shifting the diurnal cycle of parameterized deep convection over land. *Geophysical Research Letters, 36*(7), n/a-n/a. https://doi.org/10.1029/2008gl036779

Sato, T., Yoshikane, T., Satoh, M., Miltra, H., & Fujinami, H. (2008). Resolution Dependency of the Diurnal Cycle of Convective Clouds over the Tibetan Plateau in a Mesoscale Model. *Journal of the Meteorological Society of Japan, 86a*, 17-31.

This article is protected by copyright. All rights reserved.

Accepted Article

https://doi.org/10.2151/jmsj.86A.17

Song, X. L., & Zhang, G. J. (2011). Microphysics parameterization for convective clouds in a global climate model: Description and single-column model tests. *Journal of Geophysical Research-Atmospheres, 116*, D02201. https://doi.org/10.1029/2010jd014833

Stirling, A. J., & Stratton, R. A. (2012). Entrainment processes in the diurnal cycle of deep convection over land. *Quarterly Journal of the Royal Meteorological Society, 138*(666), 1135-1149. https://doi.org/10.1002/qj.1868

Storer, R. L., Griffin, B. M., Höft, J., Weber, J. K., Raut, E., Larson, V. E., et al. (2015). Parameterizing deep convection using the assumed probability density function method. *Geoscientific Model Development, 8*(1), 1-19. https://doi.org/10.5194/gmd-8-1-2015

Suselj, K., Kurowski, M. J., & Teixeira, J. (2019). A Unified Eddy-Diffusivity/Mass-Flux Approach for Modeling Atmospheric Convection. *Journal of the Atmospheric Sciences, 76*(8), 2505-2537. https://doi.org/10.1175/jas-d-18-0239.1

Tan, Z., Kaul, C. M., Pressel, K. G., Cohen, Y., Schneider, T., & Teixeira, J. (2018). An Extended Eddy-Diffusivity Mass-Flux Scheme for Unified Representation of Subgrid-Scale Turbulence and Convection. *J Adv Model Earth Syst, 10*(3), 770-800. https://doi.org/10.1002/2017MS001162

Tawfik, A. B., Lawrence, D. M., & Dirmeyer, P. A. (2017). Representing subgrid convective initiation in the Community Earth System Model. *Journal of Advances in Modeling Earth Systems, 9*(3), 1740-1758. https://doi.org/10.1002/2016ms000866

Tsushima, Y., Iga, S., Tomita, H., Satoh, M., Noda, A. T., & Webb, M. J. (2014). High cloud increase in a perturbed SST experiment with a global nonhydrostatic model including

This article is protected by copyright. All rights reserved.

Accepted Article

explicit convective processes. *Journal of Advances in Modeling Earth Systems, 6*(3), 571-585. https://doi.org/10.1002/2013ms000301

Wang, Y. C., Pan, H. L., & Hsu, H. H. (2015). Impacts of the triggering function of cumulus parameterization on warm-season diurnal rainfall cycles at the Atmospheric Radiation Measurement Southern Great Plains site. *Journal of Geophysical Research-Atmospheres, 120*(20), 10681-10702. https://doi.org/10.1002/2015jd023337

Wing, A. A., Emanuel, K., Holloway, C. E., & Muller, C. (2017). Convective Self-Aggregation in Numerical Simulations: A Review. Surveys in Geophysics, *38*(6), 1173-1197. https://doi.org/10.1007/s10712-017-9408-4

Xie, S., Wang, Y. C., Lin, W., Ma, H. Y., Tang, Q., Tang, S., et al. (2019). Improved Diurnal Cycle of Precipitation in E3SM With a Revised Convective Triggering Function. *Journal of Advances in Modeling Earth Systems, 11*(7), 2290-2310. https://doi.org/10.1029/2019ms001702

Xie, S. C., & Zhang, M. H. (2000). Impact of the convection triggering function on single-column model simulations. *Journal of Geophysical Research-Atmospheres, 105*(D11), 14983-14996. https://doi.org/Doi 10.1029/2000jd900170

Xie, S. C., Zhang, Y. Y., Giangrande, S. E., Jensen, M. P., McCoy, R., & Zhang, M. H. (2014). Interactions between cumulus convection and its environment as revealed by the MC3E sounding array. *Journal of Geophysical Research-Atmospheres, 119*(20), 11784-11808. https://doi.org/10.1002/2014jd022011

Yang, B., Qian, Y., Lin, G., Leung, L. R., Rasch, P. J., Zhang, G. J., et al. (2013). Uncertainty quantification and parameter tuning in the CAM5 Zhang-McFarlane convection scheme

This article is protected by copyright. All rights reserved.

Accepted Article

and impact of improved convection on the global circulation and climate. *Journal of Geophysical Research: Atmospheres, 118*(2), 395-415. https://doi.org/10.1029/2012jd018213

Yang, B., Wang, M., Zhang, G. J., Guo, Z., Qian, Y., Huang, A., & Zhang, Y. (2020). Simulated Precipitation Diurnal Variation With a Deep Convective Closure Subject to Shallow Convection in Community Atmosphere Model Version 5 Coupled With CLUBB. *Journal of Advances in Modeling Earth Systems, 12*(7), e2020MS002050. https://doi.org/10.1029/2020ms002050

Yu, R. C., Zhou, T. J., Xiong, A. Y., Zhu, Y. J., & Li, J. M. (2007). Diurnal variations of summer precipitation over contiguous China. *Geophysical Research Letters, 34*(1), L01704. https://doi.org/10.1029/2006gl028129

Yuan, W. H. (2013). Diurnal cycles of precipitation over subtropical China in IPCC AR5 AMIP simulations. *Advances in Atmospheric Sciences, 30*(6), 1679-1694. https://doi.org/10.1007/s00376-013-2250-9

Zhang, G. J. (2002). Convective quasi-equilibrium in midlatitude continental environment and its effect on convective parameterization. *Journal of Geophysical Research, 107*(D14). https://doi.org/10.1029/2001jd001005

Zhang, G. J., Song, X., & Wang, Y. (2019). The double ITCZ syndrome in GCMs: A coupled feedback problem among convection, clouds, atmospheric and ocean circulations. *Atmospheric Research, 229*, 255-268. https://doi.org/10.1016/j.atmosres.2019.06.023

Zhang, G. J., & Wang, H. J. (2006). Toward mitigating the double ITCZ problem in NCAR CCSM3. *Geophysical Research Letters, 33*(6), L06709.

This article is protected by copyright. All rights reserved.

https://doi.org/10.1029/2005gl025229

Zhang, K., Fu, R., Shaikh, M. J., Ghan, S., Wang, M., Leung, L. R., et al. (2017). Influence of Superparameterization and a Higher-Order Turbulence Closure on Rainfall Bias Over Amazonia in Community Atmosphere Model Version 5. *Journal of Geophysical Research: Atmospheres, 122*(18), 9879-9902. https://doi.org/10.1002/2017jd026576

Zhang, Y., & Chen, H. M. (2016). Comparing CAM5 and Superparameterized CAM5 Simulations of Summer Precipitation Characteristics over Continental East Asia: Mean State, Frequency-Intensity Relationship, Diurnal Cycle, and Influencing Factors. *Journal of Climate, 29*(3), 1067-1089. https://doi.org/10.1175/Jcli-D-15-0342.1

Accepted Article

This article is protected by copyright. All rights reserved.

Accepted Article

Table 1. A list of SCM experiments and the used convective parameterizations

Experiment	Closure
CTL_ARM95	Original ZM parameterization
REV1_ARM95	Revised parameterization with $\eta_0 = 1$
REV2_ ARM95	Revised parameterization with $\eta_0 = 0.5$
CTL_TWP06	Default ZM parameterization
REV1_TWP06	Revised parameterization with $\eta_0 = 1$
REV2_ TWP06	Revised parameterization with $\eta_0 = 0.5$

Table 2. A list of GCM experiments and the used convective parameterizations

Experiment	Closure
CTL	Original ZM parameterization
REV	Revised parameterization
REV_ULL0	Revised parameterization, but with convective launch level in the boundary layer
REV_CF0	Revised parameterization, but with convection feedback impacts turned off

This article is protected by copyright. All rights reserved.

Accepted Article

Figure captions:

Fig. 1. Assumed probability density functions (PDFs) of entrainment rate (λ) for moist convection (i.e. shallow and deep convection). λ_0 (denoted by the black solid line) corresponds to the shallowest deep convective plume in the ZM scheme. η is a scaling factor that varies with the development of convection, with the minimum entrainment rate for deep convection (i.e. $\lambda_{\min}$) set to 0.1η km^{-1} (denoted by the black dashed line).

Fig. 2. Times series of precipitation during IOPs of (a) ARM95 and (b) TWP06 from observations and simulations with the original and revised ($\eta_0 = 1$) schemes.

Fig. 3. Diurnal variations of precipitation (mm hr^{-1}) during IOP of ARM95 from observation and different simulations.

Fig. 4. Diurnal variations of the ratio of water vapor fluxes between z_0 and LCL (i.e., $\frac{\mathrm{QFX}_{z_0}}{\mathrm{QFX}_{\mathrm{lcl}}}$), deep convection memory (i.e., A), the scaling factor for entrainment rate (i.e., η/η_0), and the maximum entrainment rate assigned to deep convection (i.e., λ_0 ; km^{-1}) in the simulations of (a) REV1_ARM95 and (b) REV2_ARM95.

Fig. 5. Spatial distributions of annual mean precipitation from (a) TRMM and simulations of (b) CTL, (c) REV, and (d) REV_ULL0. Here and in the following, all the plots are based on model results from the last 10-year simulations and observations from 2001 to 2010.

Fig. 6. Meridional distributions of annual mean precipitation averaged over the eastern Pacific (160ºW–90ºW) from TRMM and different simulations.

Fig. 7. Spatial distributions of JJA (left) and DJF (right) mean precipitation from (a, b) TRMM and simulations of (c, d) CTL, (e, f) REV, and (g, h) REV_ULL0.

Fig. 8. Seasonal variation (horizontal axis) of the meridional distributions of precipitation averaged over the eastern Pacific (160ºW–90ºW) from (a) TRMM and simulations of (b) CTL and (c) REV.

Fig. 9. Same as Fig. 8 but for precipitation averaged over East Asia (105ºE–130ºE).

Fig. 10. Lag□longitude distributions of correlation coefficients of band-pass filtered (20–90 days) precipitation averaged for 10°S–10°N with precipitation averaged over the Indian Ocean region

This article is protected by copyright. All rights reserved.

(70°E–90°E, 5°S–5°N; left)) and the western Pacific region (130°E–150°E, 5°S–5°N; right) from November to April in (a, b) GPCP and simulations of (c, d) CTL, and (e, f) REV.

Fig. 11. Diurnal peak times (Local Solar Time; LST) for annual mean precipitation from (a) TRMM and simulations of (b) CTL, (c) REV, and (d) REV_ULL0. Areas with mean precipitation below 2 mm day^{-1} are masked out.

Fig. 12. Diurnal peak times (LST) for JJA mean continental precipitation from (a) TRMM and simulations of (b) CTL, (c) REV, and (d) REV_ULL0 over the US. Areas with mean precipitation below 1 mm day^{-1} are masked out.

Fig. 13. Diurnal–zonal distributions of JJA mean precipitation (normalized by daily mean value) averaged for 38°–42°N from (a) TRMM and simulations of (b) CTL, (c) REV and (d) REV_ULL0 over the US.

Fig. 14. Diurnal peak times (LST) for JJA mean continental precipitation from (a) TRMM and simulations of (b) CTL, (c) REV, (d) REV_ULL0 over East Asia. Results based on rain gauge station are shown in (e). Areas with mean precipitation magnitude below 1 mm day^{-1} are masked out.

Fig. 15. Diurnal–zonal distributions of JJA mean precipitation (normalized by daily mean value) averaged for 28°–35°N from (a) TRMM and simulations of (b) CTL, (c) REV and (d) REV_ULL0 over East Asia. Results based on rain gauge station is shown in (e).

Fig. 16. Spatial distributions of annual mean precipitation from the REV_CF0 simulation.

Fig. 17. Lag□longitude distributions of correlation coefficients of band-pass filtered (20–90 days) precipitation averaged for 10°S–10°N with precipitation averaged over the Indian Ocean region (70°E–90°E, 5°S–5°N; left)) and the western Pacific region (130°E–150°E, 5°S–5°N; right) from November to April in the REV_CF0 experiment.

Fig. 18. Diurnal peak times (LST) for JJA mean continental precipitation from the REV_CF0 experiment over the US. Areas with mean precipitation below 1 mm day^{-1} are masked out.

This article is protected by copyright. All rights reserved.

Accepted Article

Accepted Article

Figures:

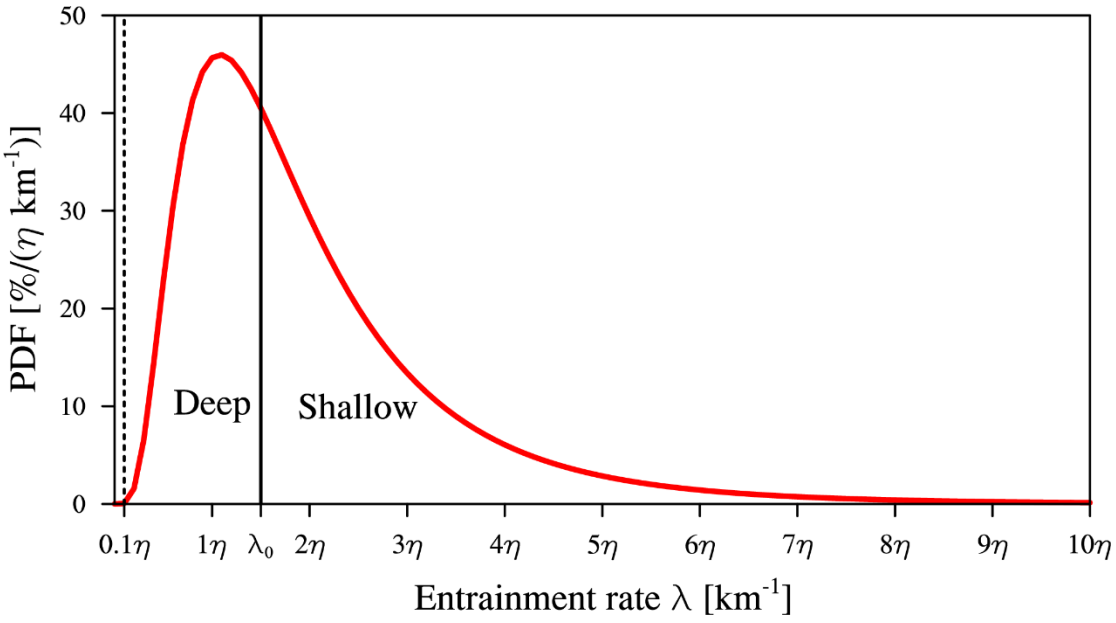

Fig. 1. Assumed probability density functions (PDFs) of entrainment rate (λ) for moist convection (i.e. shallow and deep convection). λ_0 (denoted by the black solid line) corresponds to the shallowest deep convective plume in the ZM scheme. η is a scaling factor that varies with the development of convection, with the minimum entrainment rate for deep convection (i.e. $\lambda_{\min}$) set to 0.1η km^{-1} (denoted by the black dashed line).

This article is protected by copyright. All rights reserved.

Accepted Article

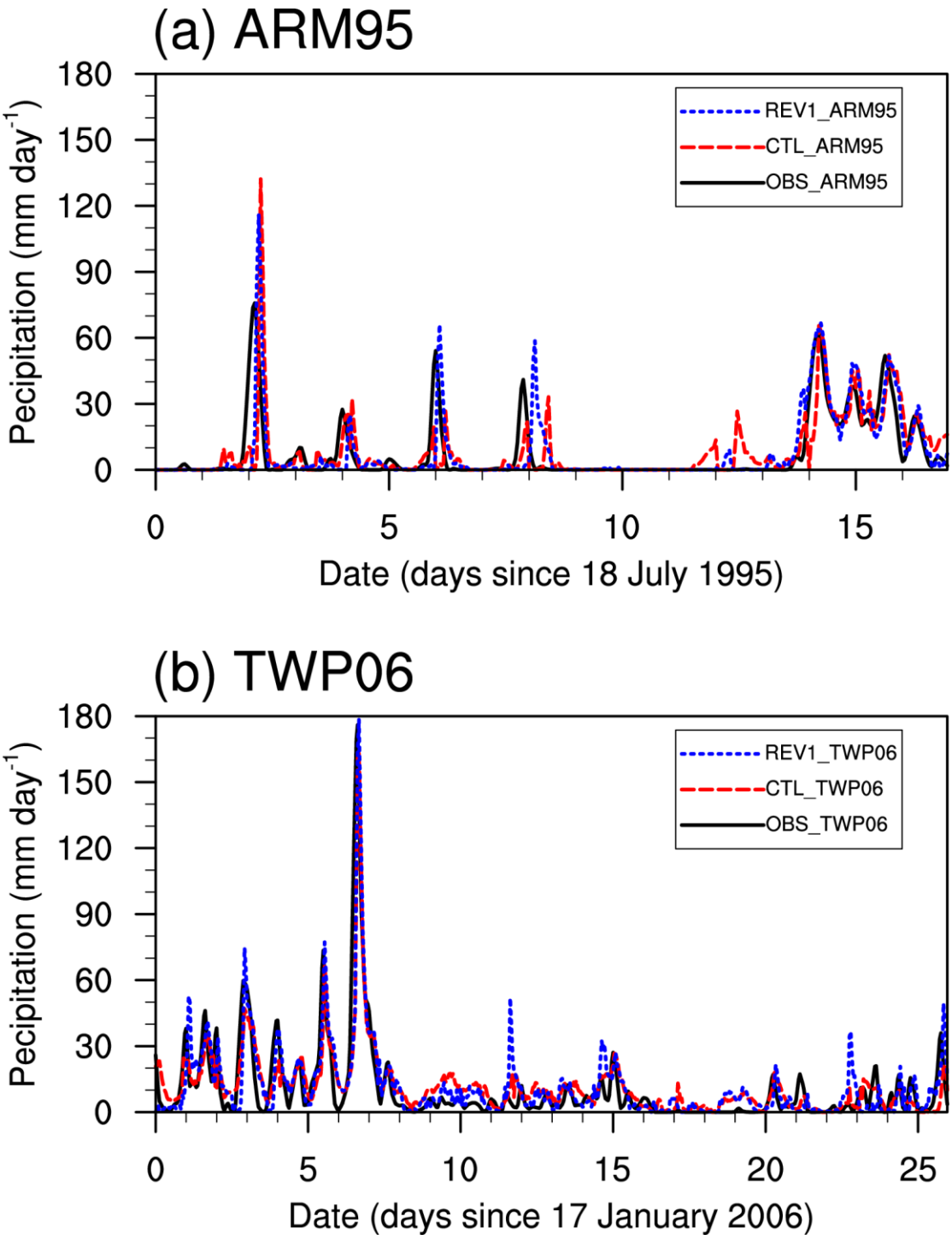

Fig. 2. Times series of precipitation during IOPs of (a) ARM95 and (b) TWP06 from observations and simulations with the original and revised ($\eta_0 = 1$) schemes.

This article is protected by copyright. All rights reserved.

Accepted Article

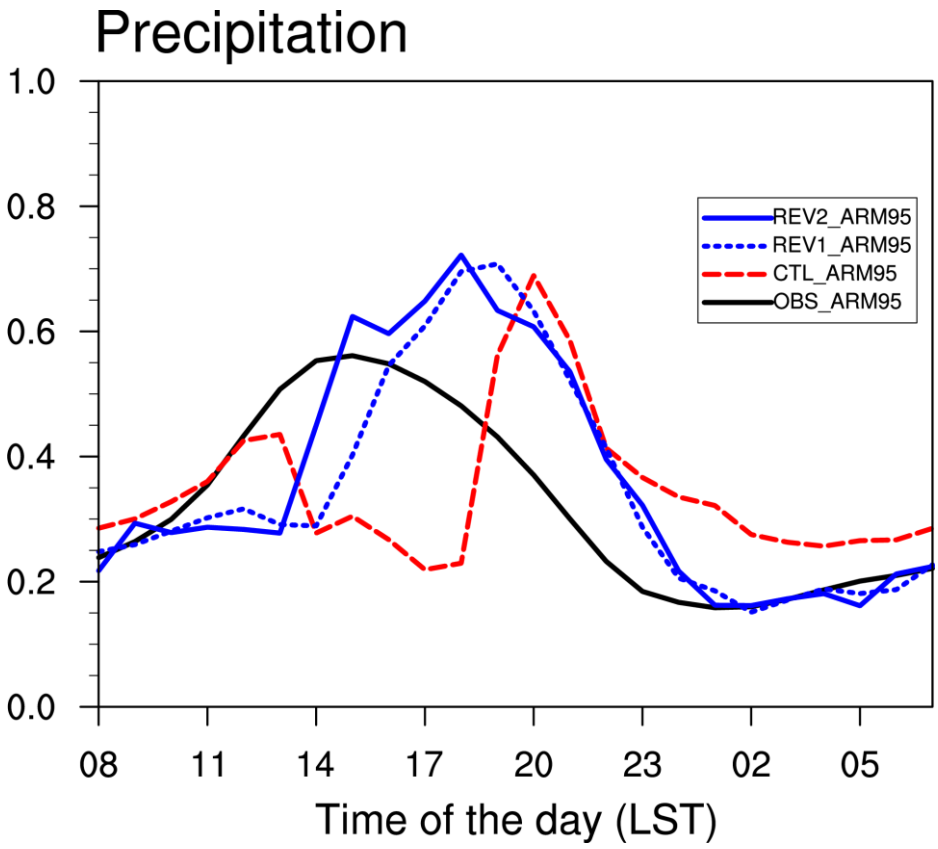

Fig. 3. Diurnal variations of precipitation (mm hr^{-1}) during IOP of ARM95 from observation and different simulations.

This article is protected by copyright. All rights reserved.

Accepted Article

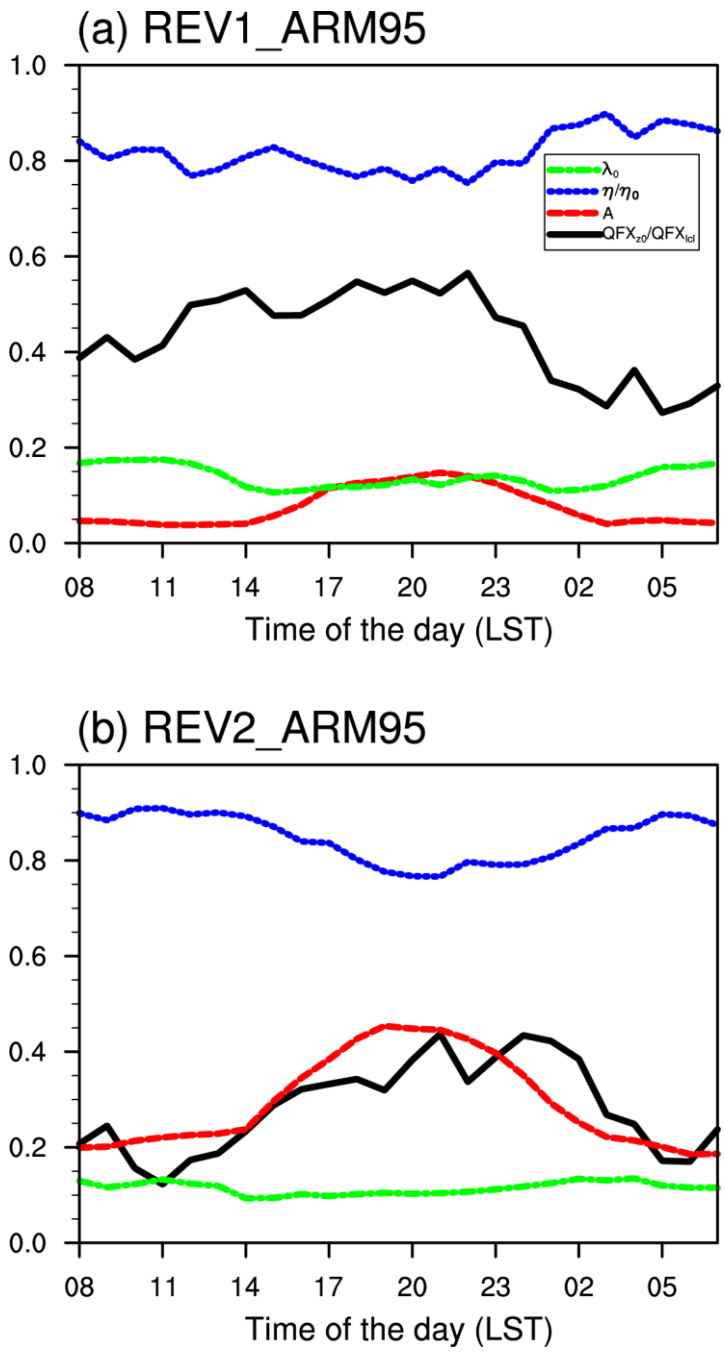

Fig. 4. Diurnal variations of the ratio of water vapor fluxes between z_0 and LCL (i.e., $\frac{\mathrm{QFX}_{z_0}}{\mathrm{QFX}_{\mathrm{lcl}}}$), deep convection memory (i.e., A), the scaling factor for entrainment rate (i.e., η/η_0), and the maximum entrainment rate assigned to deep convection (i.e., λ_0 ; km^{-1}) in the simulations of (a) REV1_ARM95 and (b) REV2_ARM95.

This article is protected by copyright. All rights reserved.

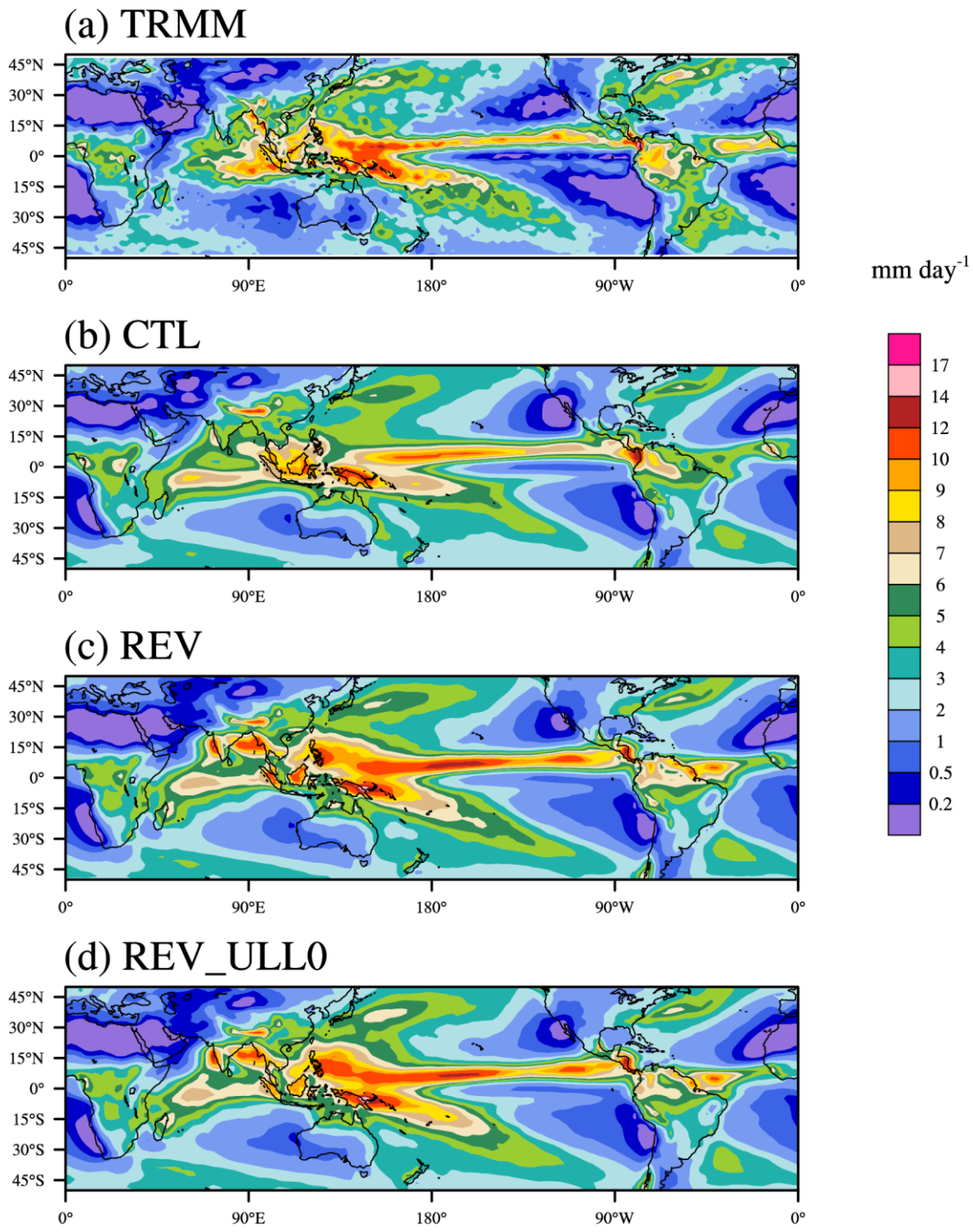

Fig. 5. Spatial distributions of annual mean precipitation from (a) TRMM and simulations of (b) CTL, (c) REV, and (d) REV_ULL0. Here and in the following, all the plots are based on model results from the last 10-year simulations and observations from 2001 to 2010.

Accepted Article

This article is protected by copyright. All rights reserved.

Accepted Article

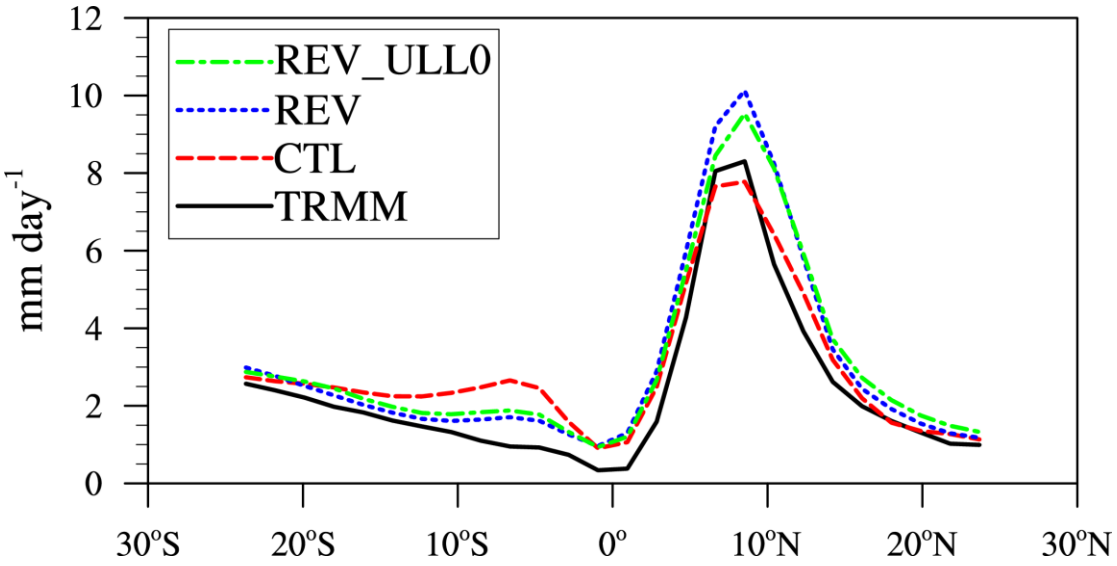

Fig. 6. Meridional distributions of annual mean precipitation averaged over the eastern Pacific (160°W–90°W) from TRMM and different simulations.

This article is protected by copyright. All rights reserved.

Accepted Article

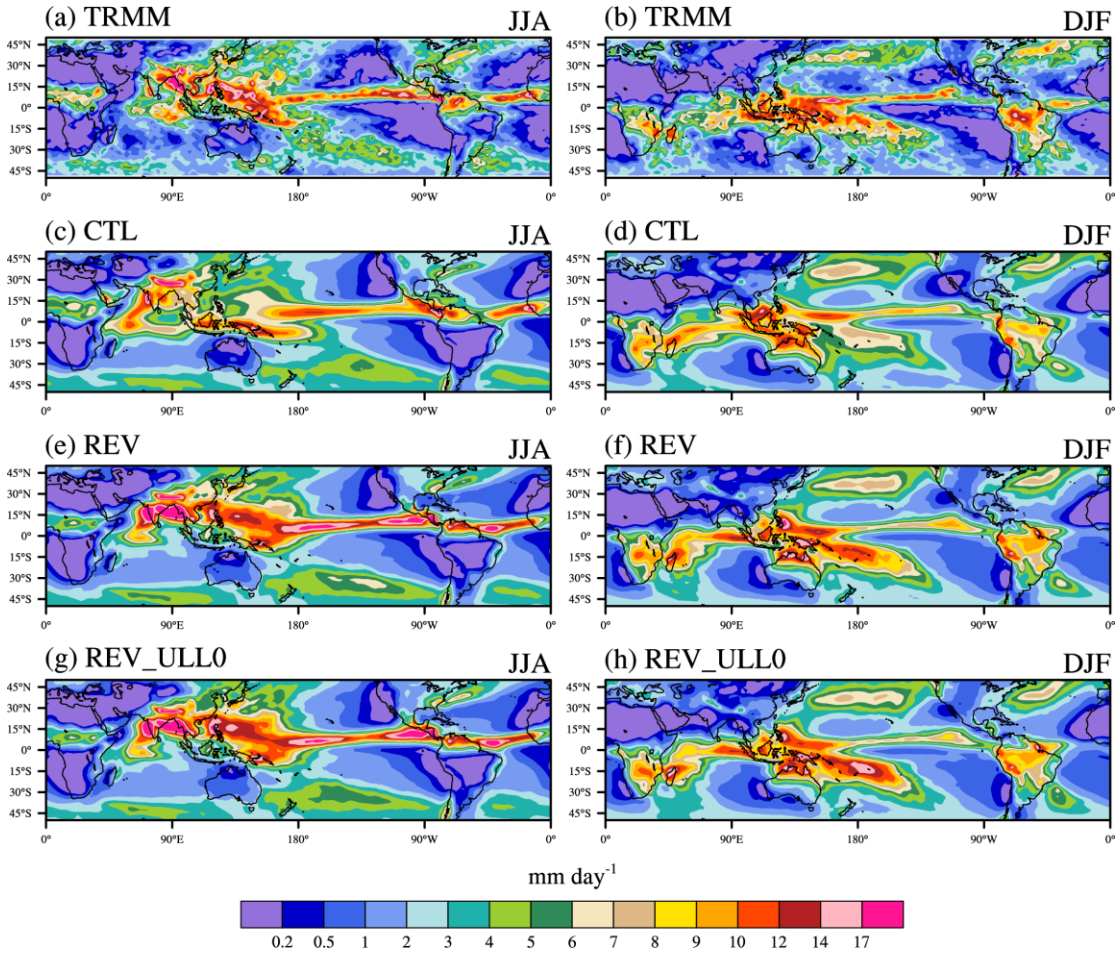

Fig. 7. Spatial distributions of JJA (left) and DJF (right) mean precipitation from (a, b) TRMM and simulations of (c, d) CTL, (e, f) REV, and (g, h) REV_ULL0.

This article is protected by copyright. All rights reserved.

Accepted Article

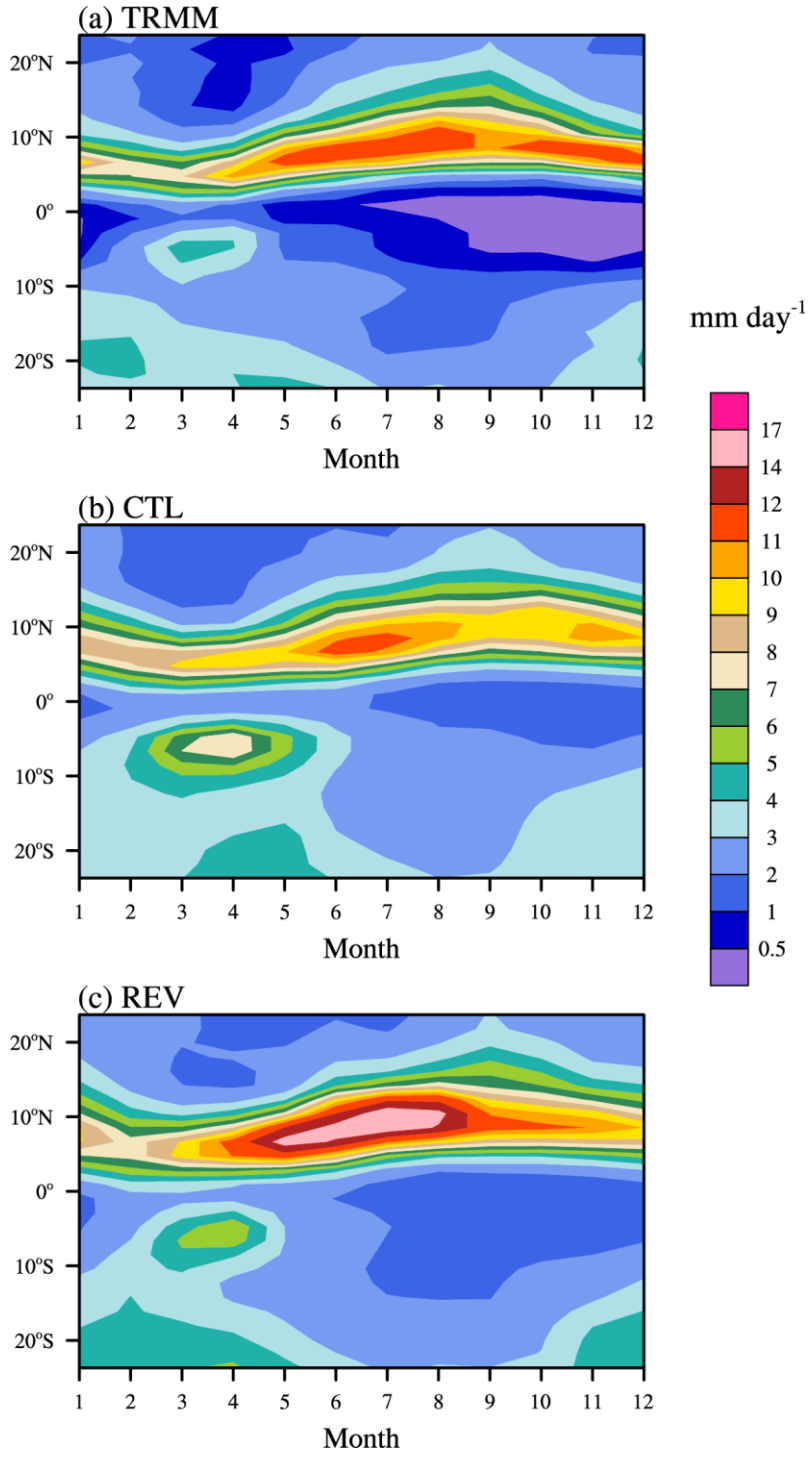

Fig. 8. Seasonal variation (horizontal axis) of the meridional distributions of precipitation averaged over the eastern Pacific (160ºW–90ºW) from (a) TRMM and simulations of (b) CTL and (c) REV.

This article is protected by copyright. All rights reserved.

Accepted Article

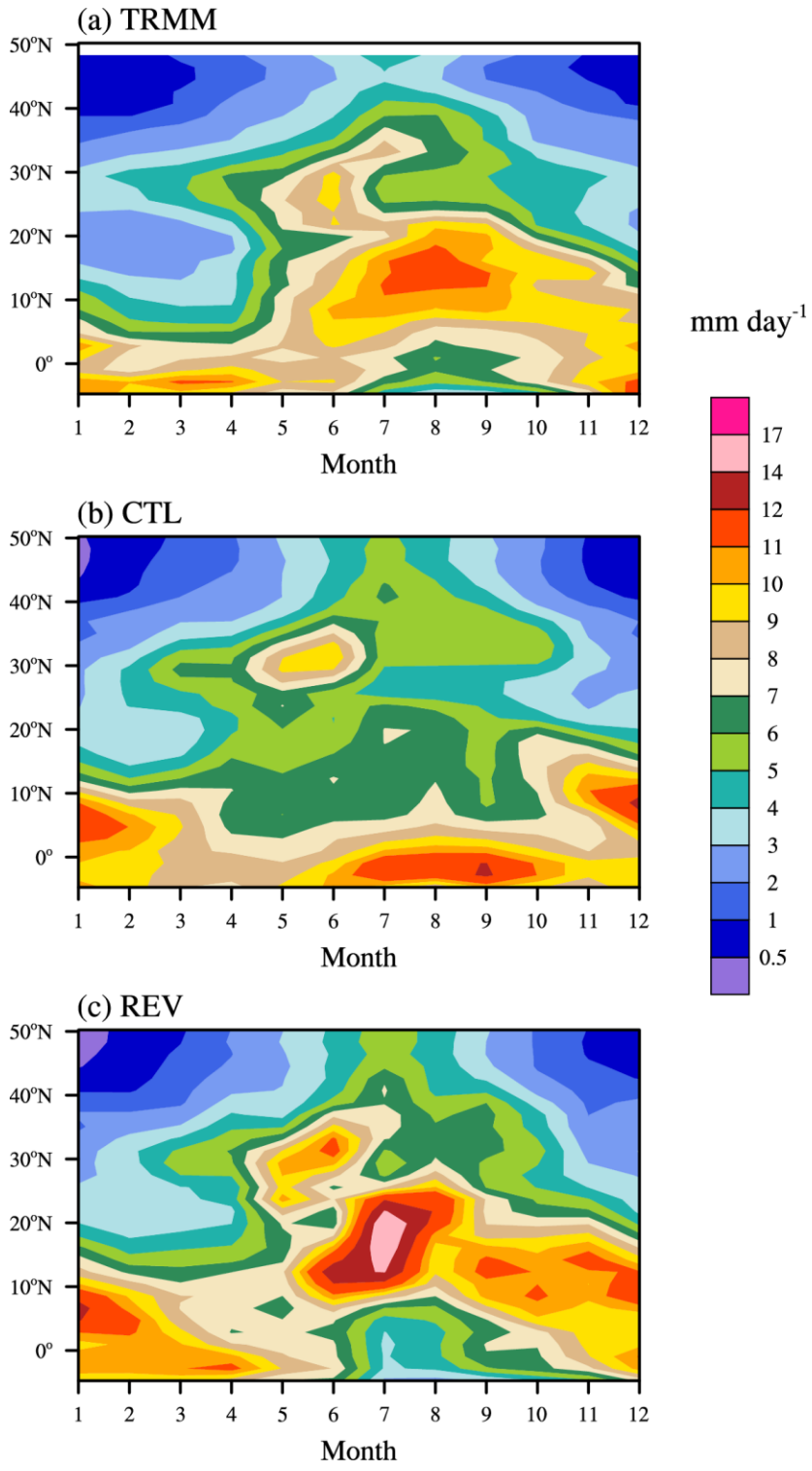

Fig. 9. Same as Fig. 8 but for precipitation averaged over East Asia (105ºE–130ºE).

This article is protected by copyright. All rights reserved.

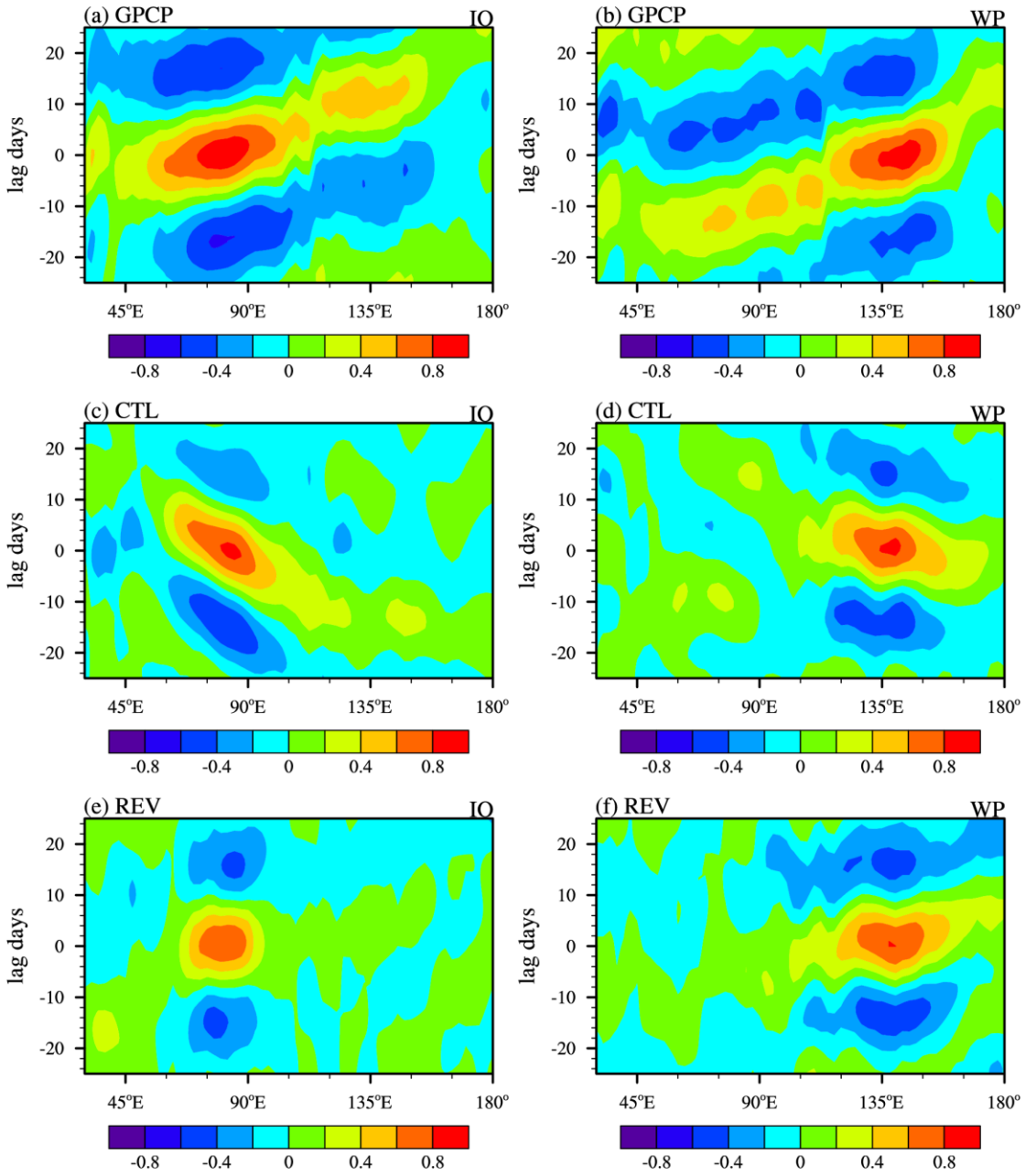

Fig. 10. Lag□longitude distributions of correlation coefficients of band-pass filtered (20–90 days) precipitation averaged for 10°S–10°N with precipitation averaged over the Indian Ocean region (70°E–90°E, 5°S–5°N; left)) and the western Pacific region (130°E–150°E, 5°S–5°N; right) from November to April in (a, b) GPCP and simulations of (c, d) CTL, and (e, f) REV.

This article is protected by copyright. All rights reserved.

Accepted Article

Accepted Article

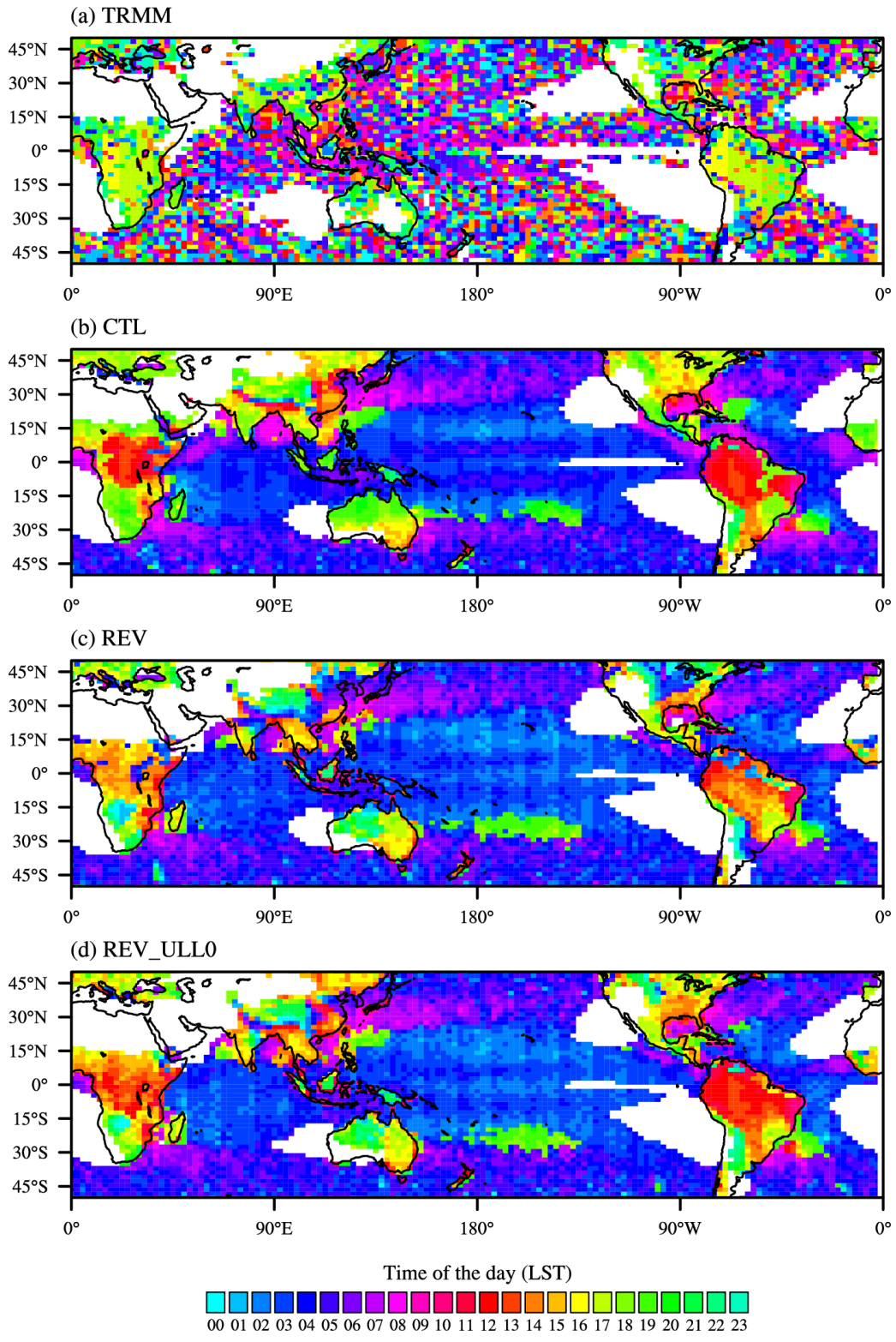

Fig. 11. Diurnal peak times (Local Solar Time; LST) for annual mean precipitation from (a) TRMM and simulations of (b) CTL, (c) REV, and (d) REV_ULL0. Areas with mean precipitation below 2 mm day^{-1} are masked out.

This article is protected by copyright. All rights reserved.

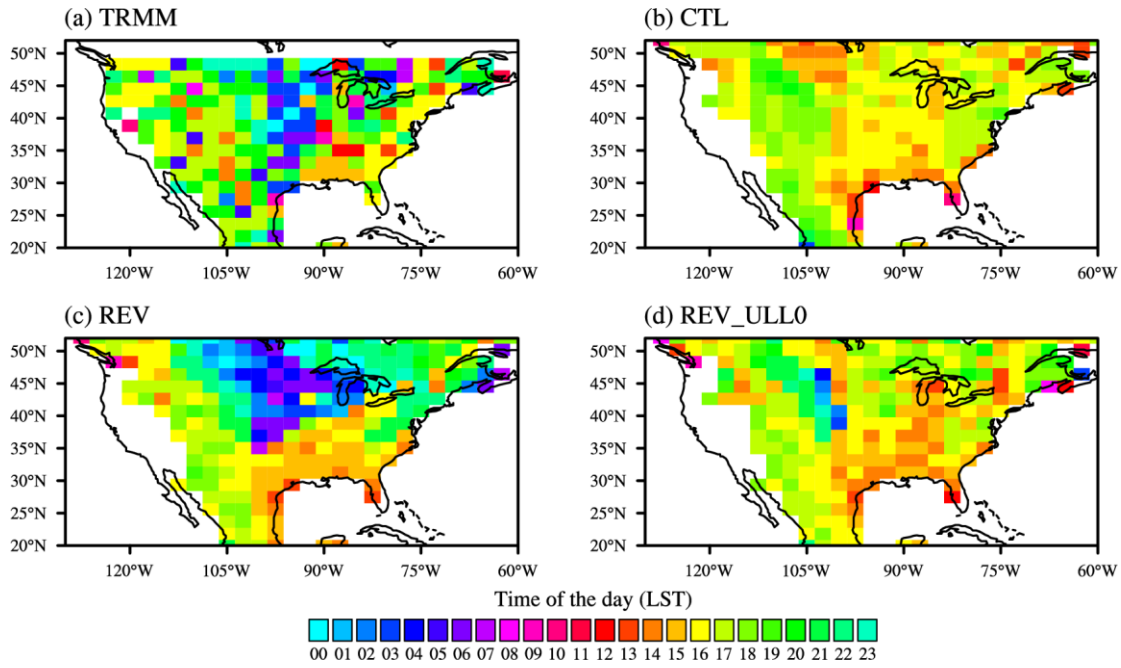

Fig. 12. Diurnal peak times (LST) for JJA mean continental precipitation from (a) TRMM and simulations of (b) CTL, (c) REV, and (d) REV_ULL0 over the US. Areas with mean precipitation below 1 mm day^{-1} are masked out.

Accepted Article

This article is protected by copyright. All rights reserved.

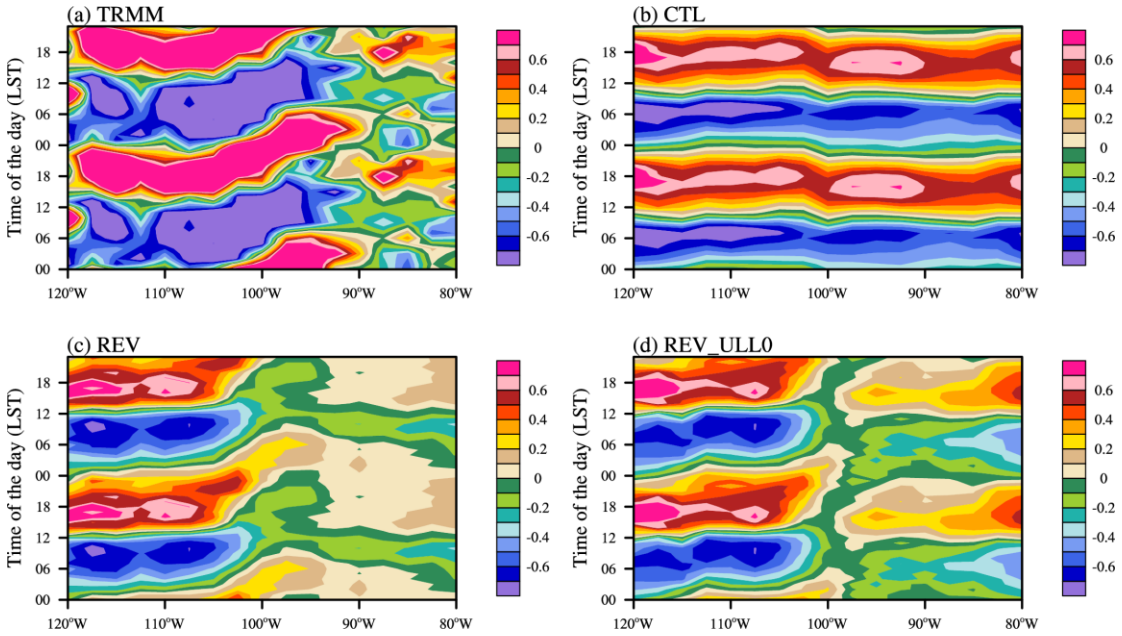

Fig. 13. Diurnal–zonal distributions of JJA mean precipitation (normalized by daily mean value) averaged for 38°–42°N from (a) TRMM and simulations of (b) CTL, (c) REV and (d) REV_ULL0 over the US.

Accepted Article

This article is protected by copyright. All rights reserved.

Accepted Article

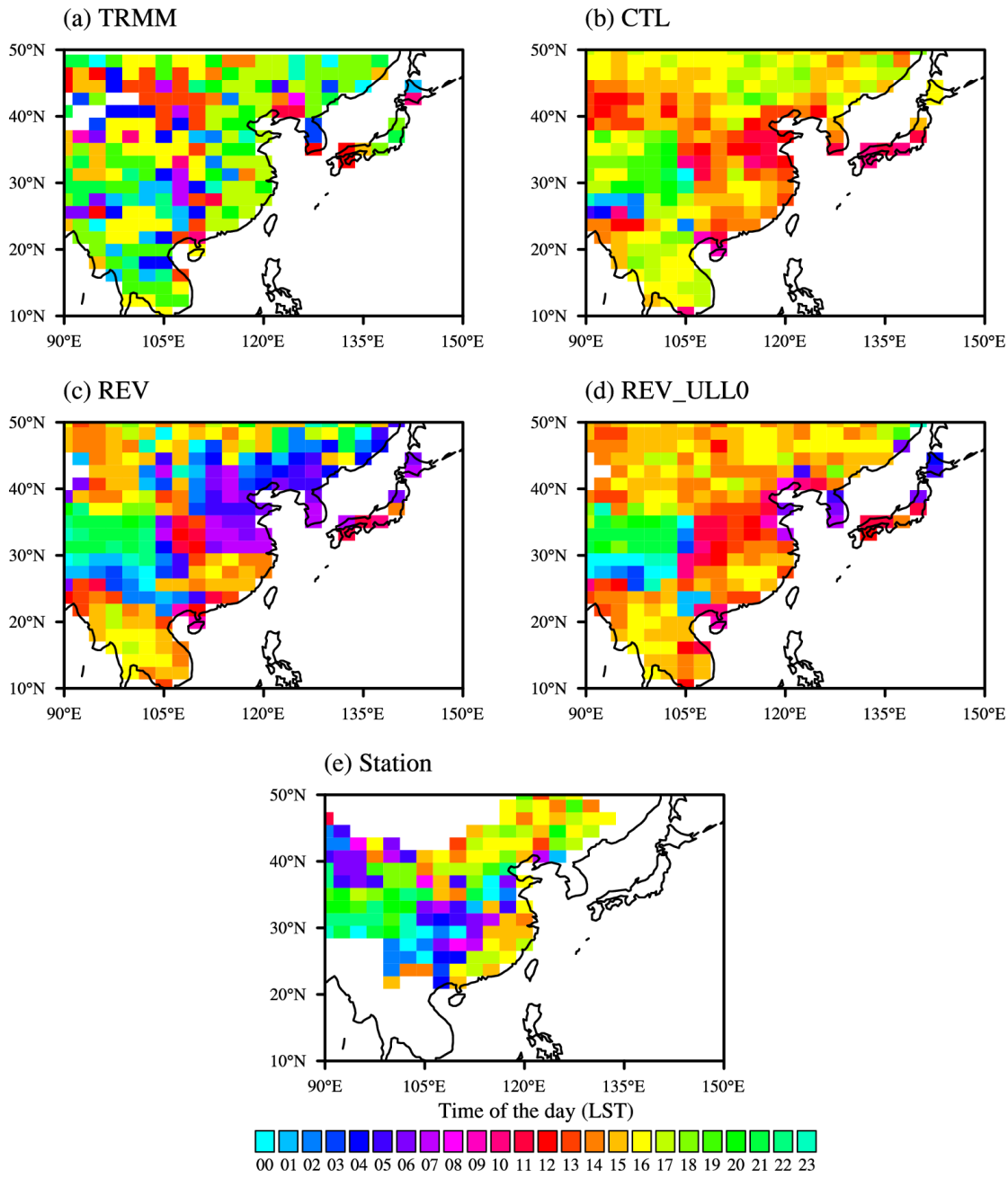

Fig. 14. Diurnal peak times (LST) for JJA mean continental precipitation from (a) TRMM and simulations of (b) CTL, (c) REV, (d) REV_ULL0 over East Asia. Results based on rain gauge station are shown in (e). Areas with mean precipitation magnitude below 1 mm day^{-1} are masked out.

This article is protected by copyright. All rights reserved.

Accepted Article

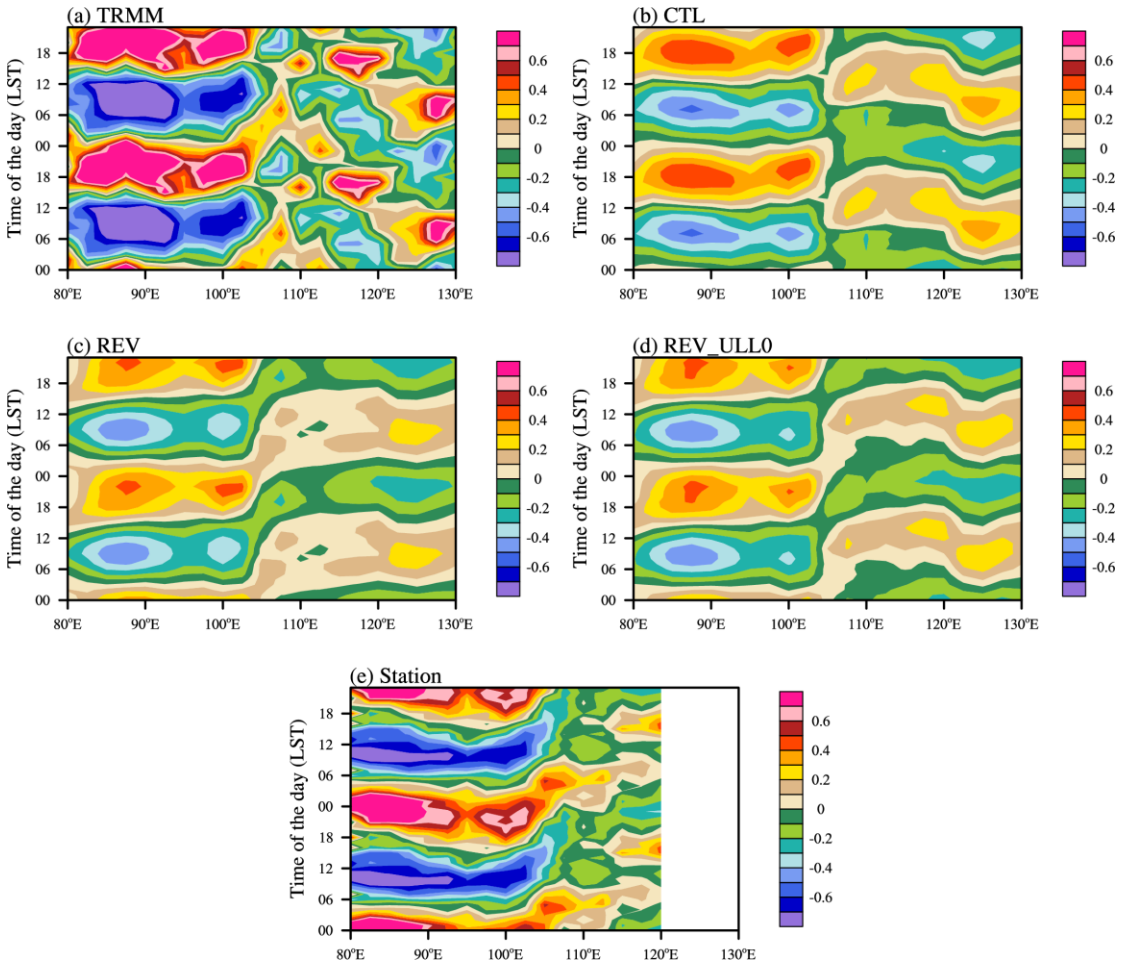

Fig. 15. Diurnal–zonal distributions of JJA mean precipitation (normalized by daily mean value) averaged for 28°–35°N from (a) TRMM and simulations of (b) CTL, (c) REV and (d) REV_ULL0 over East Asia. Results based on rain gauge station is shown in (e).

This article is protected by copyright. All rights reserved.

Accepted Article

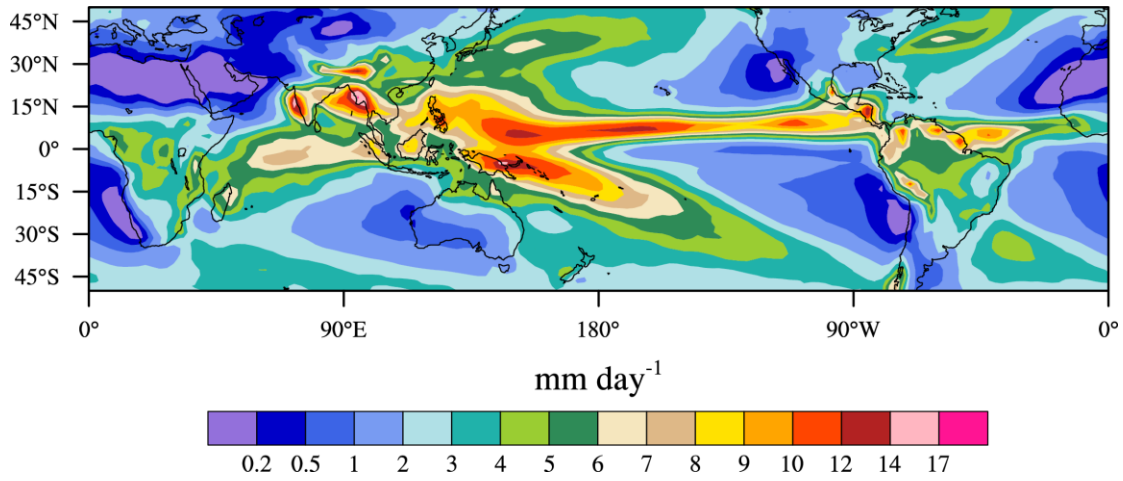

Fig. 16. Spatial distributions of annual mean precipitation from the REV_CF0 simulation.

This article is protected by copyright. All rights reserved.

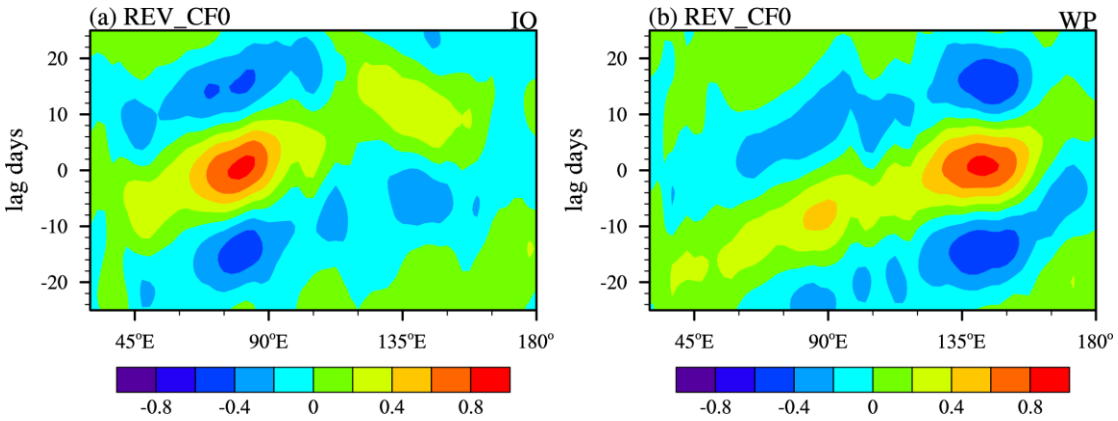

Fig. 17. Lag□longitude distributions of correlation coefficients of band-pass filtered (20–90 days) precipitation averaged for 10°S–10°N with precipitation averaged over the Indian Ocean region (70°E–90°E, 5°S–5°N; left)) and the western Pacific region (130°E–150°E, 5°S–5°N; right) from November to April in the REV_CF0 experiment.

Accepted Article

This article is protected by copyright. All rights reserved.

Accepted Article

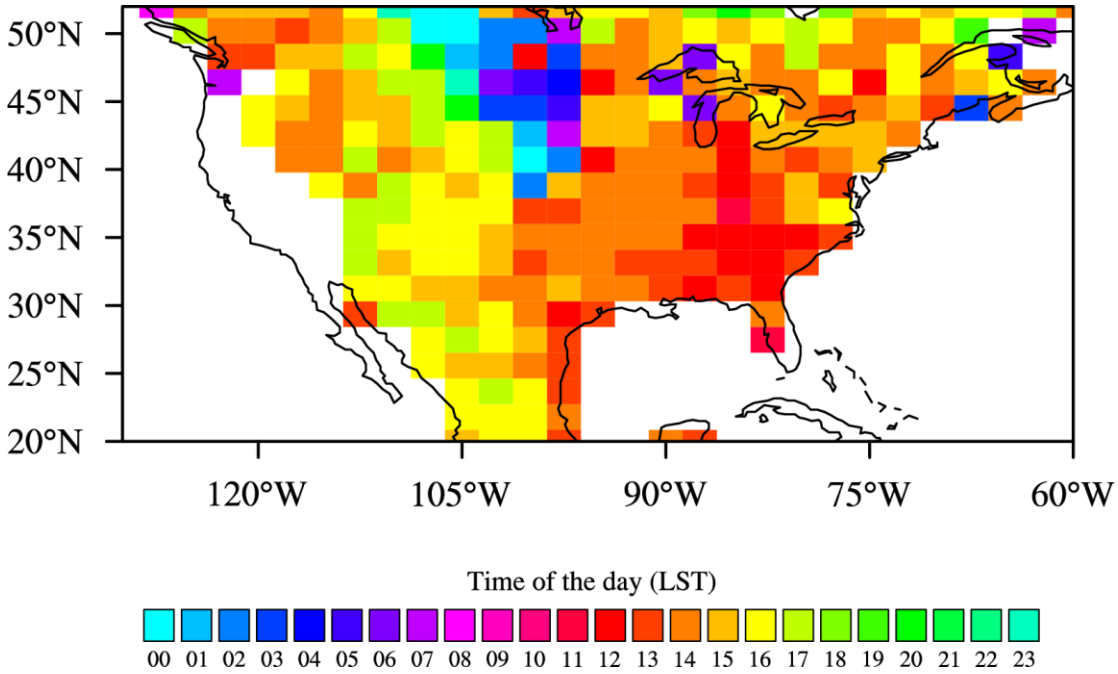

Fig. 18. Diurnal peak times (LST) for JJA mean continental precipitation from the REV_CF0 experiment over the US. Areas with mean precipitation below 1 mm day^{-1} are masked out.

This article is protected by copyright. All rights reserved.